Mixed convection flow of Magnetohydrodynamic Prandtl nanofluid containing gyrotactic microorganisms: Multi-layer neural network model

Shaik Jakeer[1], Seethi Reddy Reddisekhar Reddy[2,*], M. Lakshmi Rupa[3], Adella Aseesh Sai[4], P. Durgaprasad[4]

[1] *School of Technology, The Apollo University, Chittoor, A.P, 517127, India.*
[2]*Department of Mathematics, Koneru Lakshmaiah Education Foundation, Bowrampet, Hyderabad-500043, Telangana, India.*
[3]*Department of Mathematics, S.A.S., Vellore Institute of Technology, Vellore-632014, India.*
[4]*Division of Mathematics, SAS, Vellore Institute of Technology, Chennai-600127. India.*
** Corresponding Author E-mail:* reddyshekara43@gmail.com

Mobile: +91 7780750525

Abstract:

This study investigates the impact of activation energy on the flow behaviour of a Prandtl nanofluid that includes gyrotactic microorganisms over a stretching cylinder. This study's uniqueness is in examining Prandtl nanofluid using a non-Fourier heat and mass flow model incorporating thermal radiation. The fluid flow phenomena are defined by nonlinear differential equations and the governing equations can be solved by using an appropriate numerical technique such as bvp4c with the MATLAB solver. Based on the current investigation, the velocity outline reduces as the magnetic field values increase, while it increases concerning the curvature parameter for $\alpha = 0$ and $\alpha = \pi/2$. The temperature $\theta(\eta)$ increases as radiation values increase but decreases when the thermal relaxation parameter improves. Increased concentration relaxation, and activation energy values lead to a higher local Sherwood number. The proposed model presents significant advantages with the potential to revolutionize a wide range of applications, including biodiesel production, hydrogen fuel, oil storage techniques, geothermal energy manufacturing, base liquid mechanics, oil emulsification processes, food production, sewage systems, and serving as a substantial source of renewable energy.

Keywords: Buongiorno nanofluid model, motile microorganisms, activation energy, non-Fourier heat and mass flux, thermal radiation.

Nomenclature:	
x	Direction along the surface (m)
k_0	Permeability of the porous medium
r	Direction normal to the surface (m)
U_0	Reference velocity
l	Characteristic length
u_1 and v_1	Fluid velocity components in x and r directions (m/s)
R	Radius of the cylinder
c_p	Specific heat at constant pressure

Present address:
Adella Aseesh Sai,
School of Computer Science and Engineering, Vellore Institute of Technology, Chennai Campus – 600127, India.

k^*	Mean absorption coefficient
k	Thermal conductivity
c_m	Specific heat of dust particles
T_w	Wall temperature
l	reference length
T_∞	Temperature of the ambient fluid
A	ratio of the velocities
ε	fluid parameter
δ	elastic Parameter
γ	curvature Parameter
c	Parameter of the Prandtl fluid
υ_f	Kinematic viscosity
ρ	Density
α	Thermal diffusivity
μ_f	Dynamic viscosity of the fluid
σ^*	Stefan-Boltzmann constant
η	Similarity variable
M	magnetic parameter
K	porosity parameter
Nc	bioconvection Rayleigh number
Λ_1	thermal relaxation parameter
Λ_2	concentration relaxation parameter
Ri	mixed convection parameter
Ω	microorganisms' concentration difference parameter
ψ	Stream function
Nr	buoyancy ratio parameter
Nb	Brownian motion parameter
Rd	radiation parameter
Nt	thermophoresis parameter
Pe	bioconvection Peclet number
Le	Lewis number
Q	heat source/sink parameter
Γ	Schemical reaction parameter
E	non-dimensional activation energy
θ_w	temperature ratio parameter
Lb	bioconvection Lewis number

1. Introduction

Bioconvection is a natural phenomenon mainly involving the dispersion of self-propelled microorganisms in fluid dynamics. It is important to note that bioconvection differs from

ordinary multi-phase flows in that it involves molecules that are not driven by themselves but rather by the fluid flow, as opposed to the typical multi-phase flows. These microorganisms tend to migrate upward in the upper part of the fluid, where a concentration causes instability due to the significant density stratification. Due to the tendency of these self-propelled motile organisms to collect at the top of the fluid layer, the top layer becomes significantly denser than the bottom region, which ultimately leads to system instability [1,2]. Nanoparticles, which lack the ability to push themselves like motile microorganisms, are propelled by the Brownian movement and thermophoresis in the tiny fluids. As a result, nanoparticle mobility is unrelated to the motion of the motile bacteria. Motile microorganisms, based on impellent, may be categorized into oxytocic, gyrotactic, and negative gravities microorganisms. However, microorganisms play a significant role in theoretical and applied research in engineering, biology**,** medicine, and the environment. The ability to absorb CO2 more effectively than crops, waste treatment plants, heterogeneous catalysis, the production of biodiesel, ethanol, and fertilizers, bacterially optimized petroleum and natural gas retrieval systems, production of food, along with the chemotherapy for cancer or the utilization of enzyme biomaterials in bio-microsystems are a few examples of these applications in environmental and biological sciences [3–7]. Ahmad et al. [8] investigate the unique characteristics of hybridization tiny particles, such as manganese zinc ferrite and nickel zinc ferrite, in the bio-convective movement of mobile gyrotactic bacteria exposed to Darcy Forchheimer solutions. Dey and Chutia [9] investigated the two-phase bio-convective nanofluid flow across a vertically stretched flat surface when the dust particle volume fraction was present.

In species-level chemical reactions with low Arrhenius activation energies (AAE), mass transfer is often not possible. For the sake of this discussion, AAE will refer to the minimal quantity required for atomic or molecular interactions in a chemical system to initiate a chemical reaction. In 1889, a Swedish scientist named Svante Arrhenius coined the term "activation energy." By applying the fundamental equation for mass conservation, we can swiftly gauge the influence of mass transfer on the reaction. Various domains such as engineering oil reserves, food preparation, and geothermal theories frequently employ these AAE-containing chemical processes [10,11]. Lian et al. [12] exemplified commercial software with high-performance computational fluid dynamics (CFD) programs like Ansys CFX and chemical kinetics programs like Chemkin Ansys. Khan et al. [13] discovered the influence of AAE chemical modification on magnetohydrodynamic stagnation point flow of Casson fluids over a stretched surface. Investigating further, Khan et al. [14] explored the impact of chemical processes and AAE on the nonlinear radiation-mixed convective flow of Casson nanofluid over a stretched surface. Using an extended surface, Arrhenius activation energy, and a chemical reaction, Shafiqu et al. [15] demonstrated the 3-dimensional Maxwell nanofluid flow. While the concentration of the solute reduced the wall mass flow, the AAE rose. This decline steepens as the temperature differential between the wall and the surrounding air decreases. In the study, Reddy et al. [16] proved that activation energy affects exothermic chemical reactions involving the 3D-MHD slip flow of Powell-Eyring fluid across a thin surface.

Magnetohydrodynamics (MHD) is the study of how magnetic fields impact electrically conducting fluids such as plasmas, liquid metals, and electrolytes. Unlike classical fluid dynamics, which focuses on the interplay between fluid motion and external forces like pressure gradients, modern hydrodynamics (MHD) highlights the substantial influence of electromagnetic

forces on fluid behavior. This field unveils a myriad of unique phenomena and technical applications resulting from the strong interaction between fluid movement and magnetic fields. One of the crucial aspects of MHD is the connection between electromagnetic fields and fluid motion. When a fluid with electrical conductivity moves through a magnetic field, it generates electric currents, producing magnetic fields. These magnetic fields, in turn, exert forces on the fluid's velocity, interacting with the external magnetic field. Due to the intricate and often nonlinear dynamics arising from this interaction, MHD research is both extensive and challenging. However, it offers promising opportunities for enhancing heat transmission and controlling flow in boundary layer flows, where a thin film of fluid near a surface experiences a dense effect. MHD serves as a valuable toolkit for addressing these complexities. The boundary layer can be controlled, flow separation, drag reduction, and heat transfer may be achieved by introducing magnetic fields to a conducting fluid as it flows over a surface. Aerodynamics, marine engineering, and aerospace [17–21] are fields that may benefit from this since they focus on improving efficiency and performance by decreasing drag and increasing lift. An analytical solution was used for the first time by Crane [22] in order to investigate the boundary layer flow over a linearly stretched sheet of an incompressible viscous fluid. On top of that, MHD is quite useful for producing electricity. By harnessing the boundary layer fluxes of ionized gases or liquid metals, MHD generators can directly transform kinetic energy into electrical power. In these setups, a magnetic field is used to induce a current in the fluid, which may then be collected as electricity. The possibility for efficient and ecologically friendly energy conversion has prompted investigations into MHD power production for use on Earth and in space. Jamshed et al. [23] investigate transmission of heat by deploying a mixed nanofluid across an internally bending solar absorber. This allows for a more in-depth investigation of the solar aircraft wings in the presence of Cattaneo-Christov heat flux and porous medium. Sheikholeslami et al. [24] looked into the effects of nanofluid on photovoltaic installations and flat-plate collectors for sunlight. Waqas et al. [5] examined the bioconvection slip flow of a nanofluid called Jeffrey in the presence of a stretched sheet, using activation energy, solar radiation, and viscous dissipation principles.

Non-Newtonian fluids, unlike those following Newton's law, exhibit variable viscosity, impacting industries like pharmaceuticals and power engineering. Shear-thinning fluids, such as human blood, display decreasing viscosity under shear stress. Carreau's stress tensor expression facilitates analytical and numerical study of non-Newtonian fluids. The Prandtl fluid model, a specific type of non-Newtonian fluid, is vital for describing shear-thinning fluid behavior, aiding in understanding their properties. Biswas *et al.* [25] conducted a computer modeling study on Prandtl-nanofluid flow across infinitely vertically surfaces while a chemical reaction is present. They observed that Radiative heat increases the dispersion of temperature within a fluid by quantifying the electromagnetic radiation emitted by fluid particles and converting it into thermal radiation. Zafar *et al.* [26] revealed that the modeling of a mixed convective flow of stimulation energy including microorganisms with gyrotactic behavior over a stretched sheet using a Prandtl nanofluid. They concluded that in their observation the Prandtl nanofluid parameter increases the velocity of the fluid. Later, Hayat *et al.* [27] studied that the melting effect in Prantl-Eyring nanofluid flow over gyrotactic motile microorganism over stretching sheet in the presence of viscous dissipation. In their finding it was observed that higher melting parameter decelerates the concentration as increase in Brownian motion parameter. The references discussed regarding MHD non-Newtonian fluid models include ([28–37])

The flow across the cylinders is two-dimensional if the whole circumference is larger than the border layer's thickness. On the other hand, the radius of a thin or slender cylinder may correspond to the thickness of the boundary layer in the same order. This problem has applications in the areas of fiber coating, casting systems, metal spinning, wire drawing, flow meter design, and construction. Power, industry, transportation, and other industries all depend on fluid heating and cooling. Efficient cooling solutions are crucial for any gadgets that use a lot of energy. Due to their poor heat transfer properties, common heat transfer fluids which includes fluids such as ethylene glycol, water, and motor oil have limited heat transfer capacities. The combination of the two materials' desirable properties—fluidity and metal-like thermal conductivity—makes it an attractive heat transfer medium. Metallized materials outperform fluids in terms of heat conductivity by a factor of up to three. Wang [38] inspected the liquid movement caused by a cylinder that was extending. Heat transfer resulting from a stretching cylinder and magnetohydrodynamic flow were studied by Ishak et al. [39]. They noticed that the fluid's velocity over a stretching cylinder is slowed down by the action of a transverse magnetic field. Muhammad Bilal et al. [40] investigated the time-dependent diffusive-thermo stretching cylindrical flow in Maxwell fluid using an unsteady comparative analysis. They concluded that the thickness of the thermal boundary layer improves with the Brownian motion parameter. The modeling of applied magnetic field and thermal radiation resulting from stretched cylinder was covered by Tamoor et al. [41]. They observed that the velocity outline is improved by the mixed convection parameter.

The architecture and operation of the human brain serve as inspiration for computer models known as Artificial Neural Networks (ANNs). It has many layers of linked nodes, involving a source layer, a layer that is hidden (or layers), and an output layer. Throughout training, the network's weights are modified to let it to understand data patterns and correlations via the relationships among nodes [42–44]. Artificial Neural Networks (ANNs) are widely employed in modeling heat transfer for MHD Prandtl nanofluids, showcasing proficiency in handling intricate nonlinear relationships, predicting characteristics, and making informed decisions based on extensive datasets. This adaptability and capacity to learn from data make ANNs a potent tool specifically suited for addressing challenges inherent in MHD Prandtl nanofluid heat transfer studies. In the complete geometry or equations, sometimes the range of parameter values becomes too large or too small, making it challenging for the system to execute the solution. In such situations, the ANN model can be employed to effectively handle and overcome these numerical challenges. Their application in this domain enhances the modeling capabilities, providing an effective means to unravel nuanced heat transfer phenomena and make predictions essential for advancing scientific understanding in this specialized field.

The proposed model's main objective is to study the thermal behavior of a Prandtl nanofluid with gyrotactic microorganisms on a stretched cylinder in the presence of homogenous heat sources and sinks as well as linear thermal radiation. Additionally, the study found that no research has previously examined the effects of activation energy and Prandtl nanofluid on a porous cylinder containing gyrotactic microorganisms, including non-Fourier heat and mass flux models with thermophoresis, Brownian motion, thermal radiation, and a uniform heat source. After applying the proper self-similarity transformations to convert the system of flow temperature transport and

concentration equations into an ordinary differential system, the bvp4c with MATLAB solver is used to compute the system. Boundary value issues for ordinary differential equations (ODEs) are numerically solved by Bvp4c using the finite difference technique. The differential equations on a grid are discretized using the finite difference technique, which turns them into an algebraic system of equations. This method is well-suited for problems with complex geometries and nonlinearities. By utilizing the bvp4c solver, we ensure a reliable and efficient numerical solution to our boundary value problem, enabling accurate and stable results within the defined computational framework. Graphs and tables are used to describe the calculated outcomes. Also, we compared the present results got a good agreement with the previous published results.

To examine the issue of MHD Prandtl nanofluid flow in the presence of heat radiation, the subsequent steps were taken:

- Examining the Prandtl nanofluid's flow characteristics from multiple perspectives.
- Investigated the density of motile microorganisms and the thickness of the boundary layer.

2. Formulation of the Problem:

2.1 Basic equation of Prandtl fluid model:

This is the rheological model that Prandtl suggested [46]:

$$S = \left(\frac{A_1}{\gamma} \sin^{-1}\left(\frac{\gamma}{c} \right) \right) \tilde{A}, \tag{1}$$

In this case, the fluid parameters A_1 and c, $\tilde{A}$ is the first Rivlin-Ericksen tensor, and γ is defined as:

$$\gamma = \sqrt{\frac{1}{2} tr\tilde{A}^2} \tag{2}$$

The inverse of the sine function may be extended using Taylor's series up to the second-order approximation.

$$\sin^{-1}\left(\frac{\gamma}{c} \right) = \frac{\gamma}{c} + \frac{\gamma^3}{6c^3}, where \left| \frac{\gamma}{c} \right| < 1. \tag{3}$$

2.2 Problem description

The following is an assumption: a two-dimensional constant non-compressible and magnetically Prandtl nanofluid flow behaves on a stretchy cylinder. As seen in Figure 1, we may pretend that u_1 and v_1 stand for the components of velocity in the x and r directions, respectively. When formulating the flow, the following factors are considered: the energy of activation, thermal radiation, Buongiorno nanofluid, non-Fourier heat and mass flux model, and the consequence of binary chemical processes. It is possible to stretch the cylinder with linear axial velocity. The

direction of application of the magnetic field B_0 is perpendicular to the cylinder's axis. In addition, due to low magnetic Reynolds numbers, the produced magnetic field is rather weak in comparison to the applied magnetic field.

$$\frac{\partial(ru_1)}{\partial x}+\frac{\partial(rv_1)}{\partial r}=0, \tag{4}$$

$$\begin{aligned} &u_1\frac{\partial u_1}{\partial x}+v_1\frac{\partial u_1}{\partial r}=u_e\frac{du_e}{dx}+\frac{A_1}{\rho_f c}\frac{\partial^2 u_1}{\partial r^2}+\frac{A_1}{2\rho_f c^3}\left(\frac{\partial u_1}{\partial r}\right)^2\frac{\partial^2 u_1}{\partial r^2}+\frac{A_1}{r\rho_f c}\left(\frac{\partial u_1}{\partial r}\right)+\frac{A_1}{6r\rho_f c^3}\left(\frac{\partial u_1}{\partial r}\right)^3 \\ &+\frac{\cos\alpha}{\rho_f}\begin{Bmatrix}(1-C_\infty)\rho_f g\beta_f(T-T_\infty)-g(\rho_p-\rho_f)\\(C-C_\infty)-\gamma_1 g(\rho_m-\rho_p)(N-N_\infty)\end{Bmatrix}-\frac{\sigma_f B_0^2\sin^2\beta}{\rho_f}(u_1-u_e)-\frac{\mu}{\rho_f K_0}u_1 \end{aligned} \tag{5}$$

$$\begin{aligned} &u_1\frac{\partial T}{\partial x}+v_1\frac{\partial T}{\partial r}=\frac{\alpha}{r}\frac{\partial}{\partial r}\left(r\frac{\partial T}{\partial r}\right)+\tau D_B\left(\frac{\partial C}{\partial r}\frac{\partial T}{\partial r}\right)+\frac{\tau D_T}{T_\infty}\left(\frac{\partial T}{\partial r}\right)^2 \\ &-\lambda_1\left[u_1{}^2\frac{\partial^2 T}{\partial x^2}+v_1{}^2\frac{\partial^2 T}{\partial r^2}+v_1\frac{\partial v_1}{\partial r}\frac{\partial T}{\partial r}+v_1\frac{\partial u_1}{\partial r}\frac{\partial T}{\partial x}+u_1\frac{\partial v_1}{\partial x}\frac{\partial T}{\partial r}+u_1\frac{\partial u_1}{\partial x}\frac{\partial T}{\partial x}+2u_1v_1\frac{\partial^2 T}{\partial r\partial x}\right] \\ &-\frac{1}{(\rho C_p)_f}\frac{\partial}{\partial r}(rq_r)+\frac{Q_0}{\rho C_\rho}(T-T_\infty) \end{aligned} \tag{6}$$

$$\begin{aligned} &u_1\frac{\partial C}{\partial x}+v_1\frac{\partial C}{\partial r}=\frac{D_B}{r}\left(r\frac{\partial C}{\partial r}\right)+\frac{D_T}{rT_\infty}\frac{\partial}{\partial r}\left(r\frac{\partial T}{\partial r}\right)-K_r^2(C-C_\infty)\left(\frac{T}{T_\infty}\right)^n\exp\left(-\frac{E_a}{KT}\right) \\ &-\lambda_2\left[u_1{}^2\frac{\partial^2 C}{\partial x^2}+v_1{}^2\frac{\partial^2 C}{\partial r^2}+v_1\frac{\partial v_1}{\partial r}\frac{\partial C}{\partial r}+v_1\frac{\partial u_1}{\partial r}\frac{\partial C}{\partial x}+u_1\frac{\partial v_1}{\partial x}\frac{\partial C}{\partial r}+u_1\frac{\partial u_1}{\partial x}\frac{\partial C}{\partial x}+2u_1v_1\frac{\partial^2 C}{\partial r\partial x}\right] \end{aligned} \tag{7}$$

$$u_1\frac{\partial N}{\partial x}+v_1\frac{\partial N}{\partial r}+\frac{bW_c}{(C_w-C_\infty)}\frac{\partial}{\partial r}\left(N\frac{\partial C}{\partial r}\right)=\frac{D_m}{r}\frac{\partial}{\partial r}\left(r\frac{\partial C}{\partial r}\right) \tag{8}$$

The associated BC's are

$$\begin{aligned} &u_1=U_w, v_1=0, T=T_w, \mathrm{C}=\mathrm{C}_w, N=N_W \quad at\ r=R, \\ &u_1\to u_e, T\to T_\infty, \mathrm{C}\to C_\infty, N\to N_\infty, \ \text{at}\ r\to\infty \end{aligned} \tag{9}$$

The streaming function that was able to fulfill the equation for continuity is described as follows:

$$u_1=\frac{1}{r}\frac{\partial\psi}{\partial r}, v_1=-\frac{1}{r}\frac{\partial\psi}{\partial x}. \tag{10}$$

To change the set of Equations 4 to 9 into a nonlinearized ordinary differential equation, one may use the following transformations:

$$\eta = \frac{r^2 - R^2}{2R}\left(\frac{U_0}{\upsilon_f l}\right)^{1/2},$$

$$\psi = \left(U_w \upsilon_f x\right)^{1/2} R f(\eta), \tag{11}$$

$$\theta(\eta) = \frac{T - T_\infty}{T_w - T_\infty}, \phi(\eta) = \frac{C - C_\infty}{C_w - C_\infty}, \chi(\eta) = \frac{N - N_\infty}{N_w - N_\infty}.$$

Equation 11 satisfies the Equation 4 we alter Equations 5 through 8:

$$\begin{aligned}&\varepsilon(1+2\gamma\eta) f''' + 2\varepsilon\gamma f'' + \varepsilon\delta(1+2\gamma\eta)^2 f''^2 f''' - \left(f'^2 - A^2\right) + ff'' \\ &+ \frac{4}{3}\varepsilon\delta\gamma(1+2\gamma\eta) f''^3 + Ri\cos\alpha\left(\theta - Nr\phi - Nc\chi\right) - M\sin^2\beta\left(f' - \mathrm{A}\right) - Kf' = 0\end{aligned} \tag{12}$$

$$\begin{aligned}&\left(1 + \frac{4}{3}Rd\right)\frac{1}{\mathrm{Pr}}\left((1+2\gamma\eta)\theta'' + 2\gamma\theta'\right) + f\theta' + (1+2\gamma\eta)\left(Nb\theta'\phi' + Nt\theta'^2\right) \\ &-\Lambda_1\left(ff'\theta' + f^2\theta''\right) + Q\theta = 0\end{aligned} \tag{13}$$

$$\begin{aligned}&\frac{1}{Le}\left((1+2\gamma\eta)\phi'' + 2\gamma\phi'\right) + f\phi' + \frac{Nt}{Le\,Nb}\left((1+2\gamma\eta)\theta'' + 2\gamma\theta'\right) \\ &-\Lambda_2\left(ff'\phi' + f^2\phi''\right) - \Gamma\phi\left[1+\theta\left(\theta_w - 1\right)\right]^n e^{\frac{-E}{1+\theta(\theta_w - 1)}} = 0\end{aligned} \tag{14}$$

$$\frac{1}{Lb}\left((1+2\gamma\eta)\chi'' + 2\gamma\chi'\right) + f\chi' - \frac{Pe}{Lb}(1+2\gamma\eta)\chi'\phi' - \frac{Pe}{Lb}(\chi + \Omega)\left((1+2\gamma\eta)\phi'' + \gamma\phi'\right) = 0 \tag{15}$$

The boundary conditions are:

$$\begin{aligned}&f' = 1,\ f = 0, \theta = 1, \phi = 1, \chi = 1 \text{ at } \eta = 0, \\ &f' \to A, \theta \to 0, \phi \to 0, \chi \to 0, \text{ at } \eta \to \infty\end{aligned} \tag{16}$$

Parameters without dimensions that may be stated as:

$$A = \frac{U_\infty}{U_0}, \quad \varepsilon = \frac{A_1}{\mu_f c}, \quad \delta = \frac{U_w^2 U_0}{2c^2 \upsilon_f l}, \quad \gamma = \frac{1}{R}\sqrt{\frac{\upsilon_f l}{U_0}}, \quad M = \frac{\sigma B^2 l U_w}{\rho_f U_0}, \quad K = \frac{\mu_f l}{\rho_f k_0 U_0},$$

$$Ri = \frac{(1 - C_\infty) lg\beta_f (T_w - T_\infty)}{U_0 U_w}, \quad Nr = \frac{(\rho_p - \rho_f)(C_w - C_\infty)}{(1 - C_\infty)\rho_f \beta_f (T_w - T_\infty)}, \quad Nc = \frac{\gamma_1(\rho_m - \rho_p)(N_w - N_\infty)}{(1 - C_\infty)\rho_f \beta_f (T_w - T_\infty)},$$

$$\Lambda_1 = \frac{U_0 \lambda_1}{l}, \quad \Lambda_2 = \frac{U_0 \lambda_2}{l}, \quad Nt = \frac{\tau D_T (T_w - T_\infty)}{T_\infty \upsilon_f}, \quad Nb = \frac{\tau D_B (C_w - C_\infty)}{\upsilon_f}, \quad Rd = \frac{4\sigma^* T_\infty^3}{k^* k_f}, \quad Le = \frac{\upsilon_f}{D_B},$$

$$\Gamma = \frac{l K_r^2}{U_0}, \ E = \frac{E_a}{K T_\infty}, \ \theta_w = \frac{T_w}{T_\infty}, \ Lb = \frac{\upsilon_f}{D_m}, \ Q = \frac{l Q_0}{U_0 (\rho c_p)_f}, \ Pe = \frac{b W_c}{D_m}, \text{ and } \Omega = \frac{N_\infty}{N_w - N_\infty}.$$

3. Engineering interest

$$C_f = \frac{2\tau_w}{\rho_f U_w^2}, Nu = \frac{xq_w}{k_f\left(T_w - T_\infty\right)}, Sh = \frac{xj_w}{D_B\left(C_w - C_\infty\right)}, Nn = \frac{xq_n}{D_m\left(N_w - N_\infty\right)} \tag{17}$$

Where Surface drag force $\tau_w = \left(\frac{A_1}{c}\left(\frac{\partial u}{\partial r}\right) + \frac{A_1}{6c^3}\left(\frac{\partial u}{\partial r}\right)^3\right)_{r=R}$,

Surface heat-flux-density $q_w = -k_f\left(1 + \frac{16\sigma^* T_\infty^3}{3k^* k_f}\right)\left(\frac{\partial T}{\partial r}\right)_{r=R}$,

Surface mass-flux-density $j_w = -D_B\left(\frac{\partial C}{\partial r}\right)_{r=R}$,

Motile microorganisms-density $q_n = -D_m\left(\frac{\partial N}{\partial r}\right)_{r=R}$.

Equation 18 changes When we use the similarity changes, we get the surface friction coefficient, the heat transfer coefficient, the Sherwood number, and the density number of microbes that can move:

$$\begin{aligned}
&\frac{1}{2}C_f\,\mathrm{Re}_x^{1/2}\,X = \varepsilon f''(0) + \frac{1}{3}\varepsilon\delta\left(f''(0)\right)^3,\\
&Nu\,\mathrm{Re}_x^{-1/2}\,X^{-1} = -\left(1 + \frac{4}{3}Rd\right)\theta'(0),\\
&Sh\,\mathrm{Re}_x^{-1/2}\,X^{-1} = -\phi'(0),\\
&Nn\,\mathrm{Re}_x^{-1/2}\,X^{-1} = -\chi'(0).
\end{aligned} \tag{18}$$

Where $\mathrm{Re}_x = \frac{U_w l}{\upsilon_f}$ and $X = \sqrt{\frac{x}{l}}$.

4. Artificial neural network modelling

A state-of-the-art method for computing systems, ANN originated on the premise that the brain of people functions as a connected system of cells called neural cells. Some have noted that this procedure mimics how the human brain's neural networks evolve. When it comes to optimizing, grouping, instruction, categorization, estimation, and generalization, this model is on par with the human brain [47].

Listed below are some of the most important benefits of the ANN method:

- The ANN could be able to function well with very little hardware.
- ANN makes the complex class-distributed connecting surprisingly simple.

- To train on, you need an input vector that will tell you which results apply.
- Outcome-representing weights are acquired by iterative training.

Numerous designs are produced by combining neurons in accordance with a training rule. The strong connections between neurons are the most common cause of the layers. The ANN method consists of three separate layers: hidden, input, and outputs. The ANN receives data from the external world, processes it, and then sends it back. The machine learning components of the input layer do not modify the information before sending it to the neurons of the hidden layer. Keep in mind that the translation of information is done by the weights, connection lines, and linking the neurons. The system stores the input values and weights in a database specifically for ANN training. An ANN's construction is guided by data usage, which considers things like the ideal quantity of layers and hidden neurons.

Currently, the most popular and intriguing ANN simulation is the feed-forward neural network (FFNN) that uses a multi-layer perceptron architecture. When it comes to training FFNN, the back-propagation approach is by far the most efficient. While determining the network's output error, the backpropagation method may rearrange the weights of individual neurons in a consistent fashion, therefore reducing the output error.

The j^{th} hidden neuron receives this information as its net input:

$$y_j(x) = \sum_{i=1}^{l} W1_{ji} x_i + a_j$$

By convention, we'll refer to the layer that contains the input with the i^{th} node as x_i, the layer that is concealed with the j^{th} node as a_j, and the weight that connects the two as $W1_{ji}$.
Here is the representation of the result from the j^{th} hidden node:

$$z_j(x) = \frac{1}{1+e^{-y_j(x)}},$$

Here is the k^{th} node of the result layer:

$$o_k(x) = \sum_{j=1}^{m} W2_{kj} z_j + b_k$$

In this context, b_k refers to the influencing term at the k^{th} layer-output node, and $W2_{kj}$ is the linking weight across that node and the j^{th} hidden layer node. This study looks at surface heat as well as friction transfer rates for a cross-section of ANN result nodes, as seen in Figure 2. The constraints $A, \varepsilon, \gamma, \delta, M, Ri, Nc \,\&\, Nr$ are estimated for the samples of input nodes.

The quantity of time periods required to train the network, prevent overeating or under-setting of input parameters, and guarantee convergence of the procedure for learning determines the node count of the layer that is concealed by trial and error. To narrow the gap between the expected values of *Cf* and *Nu*, it was found that the convergence criteria used were adding one hidden layer with five cells. We trained the model using 70% of the data, validated it with 15%, and tested its predictions with the remaining 15%. Figure 3 displays the findings of the

$\left(1/2C_f \,\mathrm{Re}_x^{1/2}\, X\right)$, $\left(Nu\,\mathrm{Re}_x^{-1/2}\, X^{-1}\right)$, $\left(Sh\,\mathrm{Re}_x^{-1/2}\right)$and $\left(N_x\,\mathrm{Re}_x^{-1/2}\, X^{-1}\right)$ in the training, validation, and test sets of the ANN model. With this, ANN models have all the tools they need to mimic the intricate relationship between the two variables being simulated. The ANN model's outputs are quite consistent with the computed values.

The value of the $\left(1/2C_f \,\mathrm{Re}_x^{1/2}\, X\right)$, $\left(Nu\,\mathrm{Re}_x^{-1/2}\, X^{-1}\right)$,$\left(Sh\,\mathrm{Re}_x^{-1/2}\right)$and $\left(N_x\,\mathrm{Re}_x^{-1/2}\, X^{-1}\right)$ for the numerous values of the magnetic field $\left(M = 0.0, 1.0, 2.0\right)$, Curvature Parameter $\left(\gamma = 0.1, 0.4, 0.7\right)$, fluid parameter$\left(\varepsilon = 1.0, 1.5, 2.0\right)$, Elastic Parameter$\left(\delta = 0.0, 2.0, 4.0\right)$, thermal radiation parameter $\left(Rd = 0.0, 0.1, 2.0\right)$, ratio of the velocities parameter $\left(A = 0.5, 0.6, 0.7\right)$, ratio of specific heat$\left(\gamma = 0.5, 1.0, 1.5\right)$, Buoyancy ratio parameter $\left(Nr = 0.5, 1.0, 1.5, 2.0\right)$, heat-source/sink $\left(Q = -0.5, 0.0, 0.5\right)$ thermophoresis parameter $\left(Nt = 0.1, 0.2, 0.3\right)$, Brownian motion parameter $\left(Nb = 0.1, 0.2, 0.3\right)$, thermal relaxation parameter $\left(\Lambda_1 = 0.01, 0.1, 0.2\right)$, Lewis number$\left(Le = 1.0, 1.5, 2.0\right)$, concentration relaxation parameter $\left(\Lambda_2 = 0.01, 0.2, 0.4\right)$, activation energy parameter$\left(E = 0.0, 1.0, 2.0\right)$, Peclet number $\left(Pe = 0.0, 0.2, 0.4\right)$, bioconvection Lewis number$\left(Lb = 0.5, 1.0, 1.5\right)$, chemical reaction parameter $\left(\Gamma = 0.0, 1.0, 2.0\right)$ are shown in Tables 1 – 4. Positive results from the ANN model are shown alongside the numerical ones. So far, our work has shown that ANN can accurately estimate of skin friction, heat transmission rate, mass transfer rate and motile microorganism of local density number.

5. Results and discussion

This part aims to show precisely how the activation energy influences the flow of a Prandtl nanofluid containing gyrotactic microbes along a stretched cylinder using a Cattaneo-Christov model of mass and heat flux. Physical significance of momentum and temperature features of critical parameters on Prandtl nanofluid containing gyrotactic microorganisms velocities $f'(\eta)$, temperature $\theta(\eta)$, concentration $\phi(\eta)$, motile microorganism $\chi(\eta)$, skin friction $\left(1/2C_f \,\mathrm{Re}_x^{1/2}\, X\right)$, Nusselt number $\left(Nu\,\mathrm{Re}_x^{-1/2}\, X^{-1}\right)$, mass transfer rate $\left(Sh\,\mathrm{Re}_x^{-1/2}\, X^{-1}\right)$and motile microorganism of local density number $\left(Nn\,\mathrm{Re}_x^{-1/2}\, X^{-1}\right)$are pictured, and decoratively deliberated. The bvp4c with MATALB solver is used to solve the dimensional version of the flow, heat transport, concentration, and density of the motile microorganism's equations under certain boundary conditions. Prandtl nanofluid physical characteristics over the stretching cylinder with non-Fourier heat and mass flux of figures are compared by inclination $\left(\alpha = 0 \,\&\, \alpha = \pi/2\right)$ like solid and dotted lines, respectively. The comparative findings indicate a high level of agreement, which is displayed in Table 5. This demonstrates that the results of the numerical simulation are reliable.

Figure 4 depict how the $(M = 0.0, 1.0, 2.0)$ impacted on the $f'(\eta)$ outline in the case of $(\alpha = 0)$ and $(\alpha = \pi/2)$ correspondingly. This has been established that the $f'(\eta)$ decreases for higher values of M values for $(\alpha = 0)$ and $(\alpha = \pi/2)$. Changes in the values of the electromagnetic parameters practically cause a deviation in the Lorentz force, which in turn increases the resistance of the transport phenomenon. It is associated to inclination angle $(\alpha = 0)$, it is established that $(\alpha = \pi/2)$ has further substantial. The variations in a $f'(\eta)$ are displayed in Figure 5 on behalf of diverse values of the Curvature Parameter $(\gamma = 0.1, 0.4, 0.7)$. It is distinguished that the $f'(\eta)$ outlines upsurge by augmenting the values of the γ. Species in liquids have a lower concentration due to them disintegrate more quickly. The velocity improves as the curvature parameter enlarges, as does the thickness of the velocity boundary layer. The influence of Elastic Parameter $(\delta = 0.0, 2.0, 4.0)$ on $f'(\eta)$ is seen in Figure 6. Therefore, the $f'(\eta)$ is intensification when the δ parameter's values increase. The velocity is retarded more when the elastic parameter increases due to more recovery. It is revealed that the inclination angle $(\alpha = 0)$ has stronger influence than the inclination angle $(\alpha = \pi/2)$. Figure 7 shows the outline $f'(\eta)$ with various ratio of the velocities parameter $(A = 0.5, 0.6, 0.7)$ values approaching both inclination angle $(\alpha = 0)$ and $(\alpha = \pi/2)$. The higher values of A is augmented $f'(\eta)$. This relationship is explained by the fact that the ratio of velocities influences the acceleration of fluid flow, leading to an elevation in the velocity outline. The physical interpretation is that higher values of the stagnation parameter correspond to an augmented fluid flow velocity. The inclination angle $(\alpha = 0)$ has a bigger effect than the inclination angle $(\alpha = \pi/2)$, it is discovered.

Figure 8 demonstrates how the $(Rd = 0.0, 1.0, 2.0)$ influence on $(\alpha = 0)$ and $(\alpha = \pi/2)$ of temperature $\theta(\eta)$ variations. As the Rd -values increase, the level of heat improves $\theta(\eta)$, as shown in this graph. The inclination angle $(\alpha = \pi/2)$ has a bigger effect than the inclination angle $(\alpha = 0)$, it is discovered. There is a physical correlation between larger thermal radiation characteristics and higher temperatures as well as deeper thermal boundary layers. Figure 9 shows the results of plotting several values of the thermophoresis parameter $(Nt = 0.1, 0.2, 0.3)$ against $\theta(\eta)$, which are active aspects in the case of $(\alpha = 0)$ and $(\alpha = \pi/2)$. It is observed that $\theta(\eta)$ intensifications for boosting the Nt. The inclination angle $(\alpha = \pi/2)$ has a bigger effect than the inclination angle $(\alpha = 0)$, it is discovered. The process of thermal is responsible for this phenomenon because it exposes a larger thermal boundary layer and drags huge thermally

transmitting particles further into the fluid. The impact of the $\theta(\eta)$ on the changes in the Brownian motion parameter $(Nb = 0.1, 0.2, 0.3)$ is shown in Figure 10. It has been seen that $\theta(\eta)$ intensifications Nb increase. With an enhancement in the Brownian motion parameter, which boosts the temperature and elevates kinetic energy, nanoparticles collide with the fundamental liquid particles. Figure 11 demonstrates how the $(\Lambda_1 = 0.01, 0.1, 0.2)$ inspiration on $\theta(\eta)$ changes. An increase in the Λ_1 causes the temperature to drop, as shown in the graph.

Figure 12 is plotted for investigating the consequence of various active aspect values of the thermophoresis parameter $(Nt = 0.1, 0.2, 0.3)$ on the $\phi(\eta)$ in the case of $(\alpha = 0)$ and $(\alpha = \pi/2)$. It is detected that $\phi(\eta)$ amplifications for boosting the Nt. The inclination angle $(\alpha = 0)$ has a bigger effect than the inclination angle $(\alpha = 0)$, it is discovered. This is because a more intense thermal boundary region is exposed, and big thermally conductive particles are drawn deeper into the fluid via thermophoresis. The impact of the $\phi(\eta)$ on the changes in the (Nb) is revealed in Figure 13. It has been seen that $\phi(\eta)$ diminution for higher Nb. With an enhancement in the Brownian motion parameter, which contracts the temperature and elevates kinetic energy, nanoparticles collide with the fundamental liquid particles. Figure 14 illustrates how the concentration relaxation parameter $(\Lambda_2 = 0.01, 0.2, 0.4)$ influence on temperature $\phi(\eta)$ changes. According to this graph, the concentration is diminished by rising values in the Λ_2. Figure 15 demonstrates how the activation energy parameter $(E = 0.0, 1.0, 2.0)$ affects the concentration outline $\phi(\eta)$ in the case of $(\alpha = 0)$ and $(\alpha = \pi/2)$ into the system. It is distinguished that the $(\alpha = 0)$ and $(\alpha = \pi/2)$ outlines increase by augmenting the values of the activation energy parameter (E). A more significant activation energy causes the Arrhenius function to incline while enhancing the chemical reaction's efficacy. As a result, the nanoparticle concentration improves.

Figure 16 displays the consequence of Peclet number $(Pe = 0.0, 0.2, 0.4)$ on microorganism density $\chi(\eta)$. Consequently, greater values of the Pe parameter decrease the ambient fluid and density. The influence of Ω on microorganism density $\chi(\eta)$ is seen in Figure 17. Therefore, the microorganism density is reduced when the Ω parameter's values increase in the case of $(\alpha = 0)$ and $(\alpha = \pi/2)$ correspondingly.

Figure 18 is outlined to reveal the influence of mixed convection parameter (Ri) and elastic parameter (δ) on skin friction $(1/2C_f \operatorname{Re}_x^{1/2} X)$. It is discovered that decrees on the $(1/2C_f \operatorname{Re}_x^{1/2} X)$ nanofluid over the cylinder on the Ri and δ parameters. Figure 19 is

recognized that the rate of heat transfer $\left(Nu\,\mathrm{Re}_x^{-1/2}\,X^{-1}\right)$ is increases for the higher values of the thermophoresis parameter $\left(Nt\right)$ and radiation $\left(Rd\right)$. Figure 20 is outlined to reveal the influence of mixed convection parameter $\left(Ri\right)$ and elastic parameter $\left(\delta\right)$ on rate of heat transfer $\left(Nu\,\mathrm{Re}_x^{-1/2}\,X^{-1}\right)$. It is discovered that increase on the rate of heat transfer nanofluid over the cylinder on the Ri and δ parameters. Figure 21 is outlined to reveal the influence of concentration relaxation $\left(\Lambda_2\right)$ and activation energy E on mass transfer rate $\left(Sh\,\mathrm{Re}_x^{-1/2}\right)$.It is recognized that the higher values of the Λ_2 and E enhances the $Sh\,\mathrm{Re}_x^{-1/2}$. The consequence of the Peclet number $\left(Pe\right)$ and microorganisms concentration difference parameter $\left(\Omega\right)$ on motile microorganism of local density number $\left(N_x\,\mathrm{Re}_x^{-1/2}\,X^{-1}\right)$ is presented in Figure 22. It is illustrious that the greater values of the Pe is enriches the $N_x\,\mathrm{Re}_x^{-1/2}\,X^{-1}$ but it is decrees the higher Ω values.

6. Conclusion

The objective of this research is to analyze the effects of a uniform heat source and thermal radiation on the flow of a Prandtl nanofluid containing gyrotactic microorganisms along a stretched cylinder using a non-Fourier heat and mass flux model. Depicting the characteristics of water-based nanofluid flow after the incorporation of gyrotactic microorganisms into the mechanism is the primary objective of this study. The effect on motile microbial density of certain characteristics such as elastic, thermal relaxation, thermophoresis, Brownian motion, heat source/activation energy, Peclet number, and concentration ratio. There are tables, two-dimensional graphs, and contour figures that display the findings. This inquiry yielded the following noteworthy results:

- Velocity outline decreases for higher values of M values but it is increases to Curvature parameter for and $\left(\alpha = 0\right)$ and $\left(\alpha = \pi/2\right)$.
- The Elastic Parameter $\left(\delta\right)$ is intensification for the higher values of the $f'\left(\eta\right)$ outline.
- The temperature $\theta\left(\eta\right)$ is growths by increasing values in the Rd but it is diminished by rising values in the Λ_1.
- The concentration $\phi\left(\eta\right)$ outlines decrease by enhancing the values of the Lewis number $\left(Le\right)$.
- The microorganism density is reduced when the Ω parameter's values increase.
- Skin friction $\left(1/2C_f\,\mathrm{Re}_x^{1/2}\,X\right)$ decrees by improving the values of Ri and δ.
- The activation energy parameter enhances the solutal boundary layer thickness because it has more significance in the absence of inclination angle compared to the in the presence of inclination angle.

- Thermophoresis parameter enhances the thermal and solutal boundary layer thickness in both presence and absence of inclination angle.
- The microorganism concentration difference parameter decelerates the boundary layer thickness of density of microorganism.

References

1. Atif, S. M., Hussain, S., and Sagheer, M., "Magnetohydrodynamic stratified bioconvective flow of micropolar nanofluid due to gyrotactic microorganisms", *AIP Adv.*, **9**(2), p. 025208 (2019). https://doi.org/10.1063/1.5085742

2. Begum, N., Siddiqa, S., Sulaiman, M., et al. "Numerical solutions for gyrotactic bioconvection of dusty nanofluid along a vertical isothermal surface", *Int. J. Heat Mass Transf.*, **113**, pp. 229–236 (2017). https://doi.org/10.1016/j.ijheatmasstransfer.2017.05.071

3. Jakeer, S. and Polu, B. A. R., "Homotopy perturbation method solution of magneto-polymer nanofluid containing gyrotactic microorganisms over the permeable sheet with Cattaneo–Christov heat and mass flux model":, *Proc. Inst. Mech. Eng. Part E J. Process Mech. Eng.*, **236**(2), pp. 525–534 (2021). https://doi.org/10.1177/0954408921104899

4. Alharbi, F. M., Naeem, M., Zubair, M., et al. "Bioconvection due to gyrotactic microorganisms in couple stress hybrid nanofluid laminar mixed convection incompressible flow with magnetic nanoparticles and chemical reaction as carrier for targeted drug delivery through porous stretching sheet", *Molecules*, **26**(13), p. 3954 (2021). https://doi.org/10.3390/molecules26133954

5. Waqas, H., Kamran, T., Imran, M., et al. "MHD bioconvectional flow of Jeffrey nanofluid with motile microorganisms over a stretching sheet: solar radiation applications", *Waves in Random and Complex Media*, pp. 1–30 (2022). https://doi.org/10.1080/17455030.2022.2105418

6. Mehmood, Z. and Iqbal, Z., "Interaction of induced magnetic field and stagnation point flow on bioconvection nanofluid submerged in gyrotactic microorganisms", *J. Mol. Liq.*, **224**, pp. 1083–1091 (2016). https://doi.org/10.1016/j.molliq.2016.10.014

7. Kuznetsov, A. V., "The onset of nanofluid bioconvection in a suspension containing both nanoparticles and gyrotactic microorganisms", *Int. Commun. Heat Mass Transf.*, **37**(10), pp. 1421–1425 (2010). https://doi.org/10.1016/j.icheatmasstransfer.2010.08.015

8. Ahmad, S., Akhter, S., Imran Shahid, M., et al. "Novel thermal aspects of hybrid nanofluid flow comprising of manganese zinc ferrite MnZnFe2O4, nickel zinc ferrite NiZnFe2O4 and motile microorganisms", *Ain Shams Eng. J.*, **13**(5), p. 101668 (2022). https://doi.org/10.1016/j.asej.2021.101668

9. Dey, D. and Chutia, B., "Dusty nanofluid flow with bioconvection past a vertical stretching surface", *J. King Saud Univ. - Eng. Sci.*, **34**(6), pp. 375–380 (2022). https://doi.org/10.1016/j.jksues.2020.11.001

10. Khan, M. I., Hayat, T., Khan, M. I., et al. "Activation energy impact in nonlinear radiative

stagnation point flow of Cross nanofluid", *Int. Commun. Heat Mass Transf.*, **91**, pp. 216–224 (2018). https://doi.org/10.1016/j.icheatmasstransfer.2017.11.001

11. Hayat, T., Riaz, R., Aziz, A., et al. "Influence of Arrhenius activation energy in MHD flow of third grade nanofluid over a nonlinear stretching surface with convective heat and mass conditions", *Physica A*, **549**, p. 124006 (2020). https://doi.org/10.1016/j.physa.2019.124006

12. Lian, W., Wang, J., Wang, G., et al. "Investigation on the lignite pyrolysis reaction kinetics based on the general Arrhenius formula", *Fuel*, **268**, p. 117364 (2020). https://doi.org/10.1016/j.fuel.2020.117364

13. Khan, M. I., Qayyum, S., Hayat, T., et al. "Entropy generation minimization and binary chemical reaction with Arrhenius activation energy in MHD radiative flow of nanomaterial", *J. Mol. Liq.*, **259**, pp. 274–283 (2018). https://doi.org/10.1016/j.molliq.2018.03.049

14. Khan, M. I., Ahmad, M. W., Alsaedi, A., et al. "Entropy generation optimization in flow of non-Newtonian nanomaterial with binary chemical reaction and Arrhenius activation energy", *Physica A*, **538**, p. 122806 (2020). https://doi.org/10.1016/j.physa.2019.122806

15. Shafique, Z., Mustafa, M., and Mushtaq, A., "Boundary layer flow of Maxwell fluid in rotating frame with binary chemical reaction and activation energy", *Results Phys.*, **6**, pp. 627–633 (2016). https://doi.org/10.1016/j.rinp.2016.09.006

16. Reddy, S. R. R., Reddy, P. B. A., and Bhattacharyya, K., "Effect of nonlinear thermal radiation on 3D magneto slip flow of Eyring- Powell nanofluid flow over a slendering sheet with binary chemical reaction and Arrhenius activation energy", *Adv. Powder Technol.*, **30**(12), pp. 3203–3213 (2019). https://doi.org/10.1016/j.apt.2019.09.029

17. Reddy, S. R. R., Jakeer, S., Rupa, M. L., et al. "Two-phase analysis on radiative solar pump applications using MHD Eyring–Powell hybrid nanofluid flow with the non-Fourier heat flux model", *J. Eng. Math.*, **144**(7), pp. 1–25 (2024). https://doi.org/10.1007/s10665-023-10306-2

18. Jakeer, S., Shanmugapriyan, N., and Reddy, S. R. R., "Numerical simulation of bio-magnetic nanofluid flow in the human circulatory system", *Numer. Heat Transf. Part A Appl.*, pp. 1–29 (2024). https://doi.org/10.1080/10407782.2024.2304046

19. Khan, N. S., Hussanan, A., Kumam, W., Kumam, P., et al. "Accessing the thermodynamics of Walter-B fluid with magnetic dipole effect past a curved stretching surface", *ZAMM - J. Appl. Math. Mech. / Zeitschrift für Angew. Math. und Mech.*, **103**(8), p. e202100112 (2023). https://doi.org/10.1002/zamm.202100112

20. Metwally, A. S. M., Khalid, A., Khan, A. A., et al. "Radiation consequences on Sutterby fluid over a curved surface", *J. Eng. Thermophys.*, **31**(2), pp. 315–327 (2022). https://doi.org/10.1134/S1810232822020126

21. Reddy, S. R. R., Sekhar, K. R., Charupalli, S. K., et al. "Impact of Arrhenius activation energy on magnetic nanofluid flow over a slendering stretchable sheet with nonlinear radiative heat transfer: A machine learning algorithm", *Numer. Heat Transf. Part B*

Fundam., pp. 1–23 (2024). https://doi.org/10.1080/10407790.2024.2333942

22. Crane, L. J., "Flow past a stretching plate", *Zeitschrift für Angew. Math. und Phys. ZAMP*, **21**(4), pp. 645–647 (1970). https://doi.org/10.1007/BF01587695

23. Jamshed, W., Nisar, K. S., Ibrahim, R. W., et al. "Thermal expansion optimization in solar aircraft using tangent hyperbolic hybrid nanofluid: a solar thermal application", *J. Mater. Res. Technol.*, **14**, pp. 985–1006 (2021). https://doi.org/10.1016/j.jmrt.2021.06.031

24. Sheikholeslami, M., Farshad, S. A., Ebrahimpour, Z., et al. "Recent progress on flat plate solar collectors and photovoltaic systems in the presence of nanofluid: A review", *J. Clean. Prod.*, **293**, p. 126119 (2021). https://doi.org/10.1016/j.jclepro.2021.126119

25. Biswas, R., Falodun, B. O., Islam, N., et al. "Computational modeling of Prandtl-nanofluid flow using exponentially vertical surface in terms of chemical reaction", *Eng. Reports*, **6**(4), p. e12747 (2024). https://doi.org/10.1002/eng2.12747

26. Zafar, S. S., Alfaleh, A., Zaib, A., et al. "Simulation of Prandtl Nanofluid in the Mixed Convective Flow of Activation Energy with Gyrotactic Microorganisms: Numerical Outlook Features of Micro-Machines", *Micromachines*, **14**(3), p. 559 (2023). https://doi.org/10.3390/mi14030559

27. Hayat, T., Ullah, I., Muhammad, K., et al. "Gyrotactic microorganism and bio-convection during flow of Prandtl-Eyring nanomaterial", *Nonlinear Eng.*, **10**(1), pp. 201–212 (2021). https://doi.org/10.1515/nleng-2021-0015

28. Shi, Q. H., Shabbir, T., Mushtaq, M., et al. "Modelling and numerical computation for flow of micropolar fluid towards an exponential curved surface: a Keller box method", *Sci. Rep.*, **11**(1), pp. 1–13 (2021). https://doi.org/10.1038/s41598-021-95859-x

29. Farooq, U., Waqas, H., Fatima, N., et al. "Computational framework of cobalt ferrite and silver-based hybrid nanofluid over a rotating disk and cone: a comparative study", *Sci. Rep.*, **13**(1), pp. 1–13 (2023). https://doi.org/10.1038/s41598-023-32360-7

30. Shah, Z., Shutaywi, M., Dawar, A., et al. "Impact of Cattaneo-Christov heat flux on non-isothermal convective micropolar fluid flow in a hall MHD generator system", *J. Mater. Res. Technol.*, **9**(3), pp. 5452–5462 (2020). https://doi.org/10.1016/j.jmrt.2020.03.071

31. Shah, Z., Khan, A., Khan, W., et al. "Micropolar gold blood nanofluid flow and radiative heat transfer between permeable channels", *Comput. Methods Programs Biomed.*, **186**, p. 105197 (2020). https://doi.org/10.1016/j.cmpb.2019.105197

32. Farooq, U., Imran, M., Fatima, N., et al. "Cattaneo-Christov heat flux model in radiative flow of (Fe3O4– TiO2/Transformer oil) and (Cu– TiO2/Transformer oil) magnetized hybrid nanofluids past through double rotating disks", *Case Stud. Therm. Eng.*, **45**, p. 102905 (2023). https://doi.org/10.1016/j.csite.2023.102905

33. Qayyum, M., Afzal, S., Saeed, S. T., et al. "Unsteady hybrid nanofluid (Cu-UO2/blood) with chemical reaction and non-linear thermal radiation through convective boundaries: An application to bio-medicine", *Heliyon*, **9**, p. e16578 (2023). https://doi.org/10.1016/j.heliyon.2023.e16578

34. Adnan, AlBaidani, M.M., Mishra, N. K., et al. “Numerical analysis of magneto-radiated annular fin natural-convective heat transfer performance using advanced ternary nanofluid considering shape factors with heating source”, *Case Stud. Therm. Eng.*, **44**, p. 102825 (2023). https://doi.org/10.1016/j.csite.2023.102825

35. Reddy, S. R. R., “Bio-magnetic pulsatile flow of Ti-alloy-Au/blood couple stress hybrid nanofluid in a rotating channel”, *Waves in Random and Complex Media*, pp. 1–24 (2022). https://doi.org/10.1080/17455030.2022.2150333

36. Reddy, S. R. R., “Entropy generation on biomagnetic gold-copper/blood hybrid nanofluid flow driven by electrokinetic force in a horizontal irregular channel with bioconvection phenomenon”, *Proc IMechE Part CJ Mech. Eng. Sci.*, **237**(7), pp. 1631–1646 (2023). https://doi.org/10.1177/09544062221130018

37. Shahzad, A., Imran, M., Tahir, M., et al. “Brownian motion and thermophoretic diffusion impact on Darcy-Forchheimer flow of bioconvective micropolar nanofluid between double disks with Cattaneo-Christov heat flux”, *Alexandria Eng. J.*, **62**, pp. 1–15 (2023). https://doi.org/10.1016/j.aej.2022.07.023

38. Wang, C. Y., “Fluid flow due to a stretching cylinder”, *Phys. Fluids*, **31**(3), pp. 466–468 (1988). https://doi.org/10.1016/j.ijft.2023.100444

39. Ishak, A., Nazar, R., and Pop, I., “Magnetohydrodynamic (MHD) flow and heat transfer due to a stretching cylinder”, *Energy Convers. Manag.*, **49**(11), pp. 3265–3269 (2008). https://doi.org/10.1016/j.enconman.2007.11.013

40. Bilal, M., Saeed, A., Selim, M. M., et al. “Comparative numerical analysis of Maxwell’s time-dependent thermo-diffusive flow through a stretching cylinder”, *Case Stud. Therm. Eng.*, **27**, p. 101301 (2021). https://doi.org/10.1016/j.csite.2021.101301

41. Tamoor, M., Kamran, M., Rehman, S., et al. “Modelling of applied magnetic field and thermal radiations due to the stretching of cylinder”, *Processes*, **9**(6), p. 1077 (2021). https://doi.org/10.3390/pr9061077

42. Jakeer, S., Rupa, M. L., Reddy, S. R. R., et al. “Artificial neural network model of non-Darcy MHD Sutterby hybrid nanofluid flow over a curved permeable surface: Solar energy applications”, *Propuls. Power Res.*, **12**(3), pp. 410–427 (2023). https://doi.org/10.1016/j.jppr.2023.07.002

43. Reddy, S. R. R., Jakeer, S., and Rupa, M. L., “ANN model of three-dimensional micropolar dusty hybrid nanofluid flow with coriolis force: biomedical applications”, *Indian J. Phys.*, **97**(13), pp. 3801–3825 (2023). https://doi.org/10.1007/s12648-023-02737-5

44. Zhao, T. H., Khan, M. I., and Chu, Y. M., “Artificial neural networking (ANN) analysis for heat and entropy generation in flow of non-Newtonian fluid between two rotating disks”, *Math. Methods Appl. Sci.*, pp. 1–19 (2021). https://doi.org/10.1002/mma.7310

45. Vajravelu, K., Prasad, K. V., and Santhi, S. R., “Axisymmetric magneto-hydrodynamic (MHD) flow and heat transfer at a non-isothermal stretching cylinder”, *Appl. Math. Comput.*, **219**(8), pp. 3993–4005 (2012). https://doi.org/10.1016/j.amc.2012.10.034

46. Shah, S. A. A., Ahammad, N. A., Ali, B., et al. "Significance of bio-convection, MHD, thermal radiation and activation energy across Prandtl nanofluid flow: A case of stretching cylinder", *Int. Commun. Heat Mass Transf.*, **137**, p. 106299 (2022). https://doi.org/10.1016/j.icheatmasstransfer.2022.106299

47. Anand, A. V., Ali, R., Jakeer, S., et al. "Entropy-optimized MHD three-dimensional solar slendering sheet of micropolar hybrid nanofluid flow using a machine learning approach", *J. Therm. Anal. Calorim.* (2023). https://doi.org/10.1007/s10973-023-12600-8

Biographies

Dr. Shaik Jakeer is an Assistant Professor in the Department of Mathematics, School of Technology, The Apollo University, Chittoor India. Obtained an M.Sc. in Applied Mathematics from Sri Venkateswara University in Tirupathi, India, and a Ph.D. in Fluid Dynamics from VIT University, Vellore, Tamil Nadu. He has extensive expertise conducting research and teaching. His research focuses on fluid dynamics, heat, and mass transport, nanofluids, magnetohydrodynamics, and hybrid nanofluids. He has over 35 research publications to his credit in peer-reviewed international journals. He gave multiple paper presentations at national and international conferences. In addition, he has reviewed around 50 articles from different international publishers.

Dr. Seethi Reddy Reddisekhar Reddy is an Assistant Professor of Mathematics at K L University, India. He holds a Ph.D. in Fluid Dynamics from the Vellore Institute of Technology (2021) and a postgraduate (M.Sc.) degree in Applied Mathematics from Sri Venkateswara University, Tirupati (2015). His research interests span Heat & Mass Transfer, Magnetohydrodynamics, Thermal Radiation, Numerical Simulation, Entropy Generation, Artificial Neural Networks, peristaltic pumps, Non-Newtonian Fluids, and Nanofluid flow. He teaches subjects like Numerical Methods, Differential Equations, Real Analysis, Complex Analysis, and Linear Algebra for Science and Engineering courses. Dr. Reddisekhar Reddy has published 44 peer-reviewed research papers and one book chapter and he also actively participates in national and international conferences.

Ms. M. Lakshmi Rupa is a research scholar in the Department of Mathematics at the School of Advanced Sciences, Vellore Institute of Technology (VIT), India. She holds an M.Sc. in Mathematics from Sri Venkateswara University in Tirupati. Currently, she is pursuing her Ph.D. in the area of fractional calculus, with a focus on fluid dynamics, magnetohydrodynamics, hybrid nanofluids, and fractional differential equations. With over 9 research publications in peer-reviewed international journals, her work significantly contributes to our understanding of complex phenomena in these fields.

Mr. Adella Aseesh Sai is a student in the Department of Computer Science and Engineering, Vellore Institute of Technology, Chennai, India. He is pursuing his Bachelor of Technology in Computer Science with Specialization in Artificial Intelligence and Machine Learning. He has been extensively involved in creating applications of deep learning and researching them. In addition to his academic achievements, he has completed internships at prestigious institutions

such as IIT Kharagpur and the Advanced Systems Laboratory (ASL), Defense Research and Development Organization (DRDO).

Dr. P. Durgaprasad is an Assistant Professor in the Department of Mathematics, Vellore Institute of Technology, Chennai, India. Obtained an M.Sc. in Applied Mathematics from Sri Venkateswara University in Tirupathi, India; at the same university, the author also completed an M. Phil., and Ph. D. He has extensive expertise conducting research and teaching. His research focuses on fluid dynamics, heat, and mass transport, nanofluids, magnetohydrodynamics, and hybrid nanofluids. He has over 50 research publications to his credit in peer-reviewed national and international journals. He gave multiple paper presentations at national and international conferences. In addition, he has reviewed around 98 articles from different international publishers.

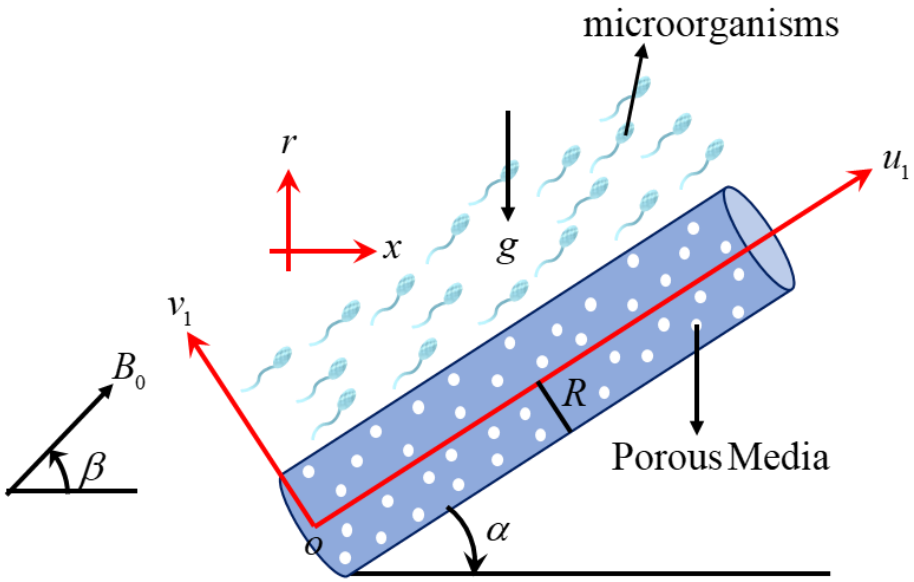

Figure 1 Geometry of the problem.

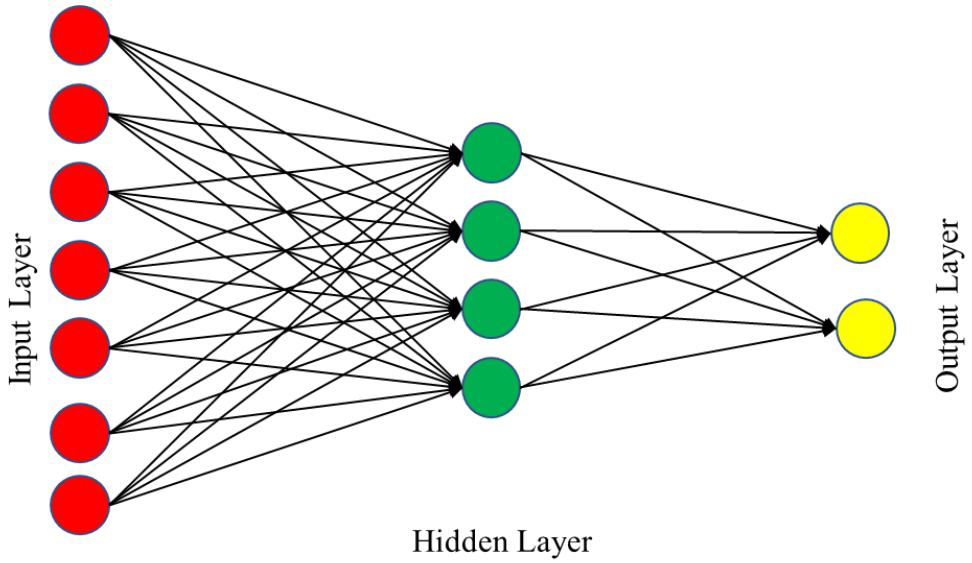

Figure 2 An ANN model with several layers is shown schematically.

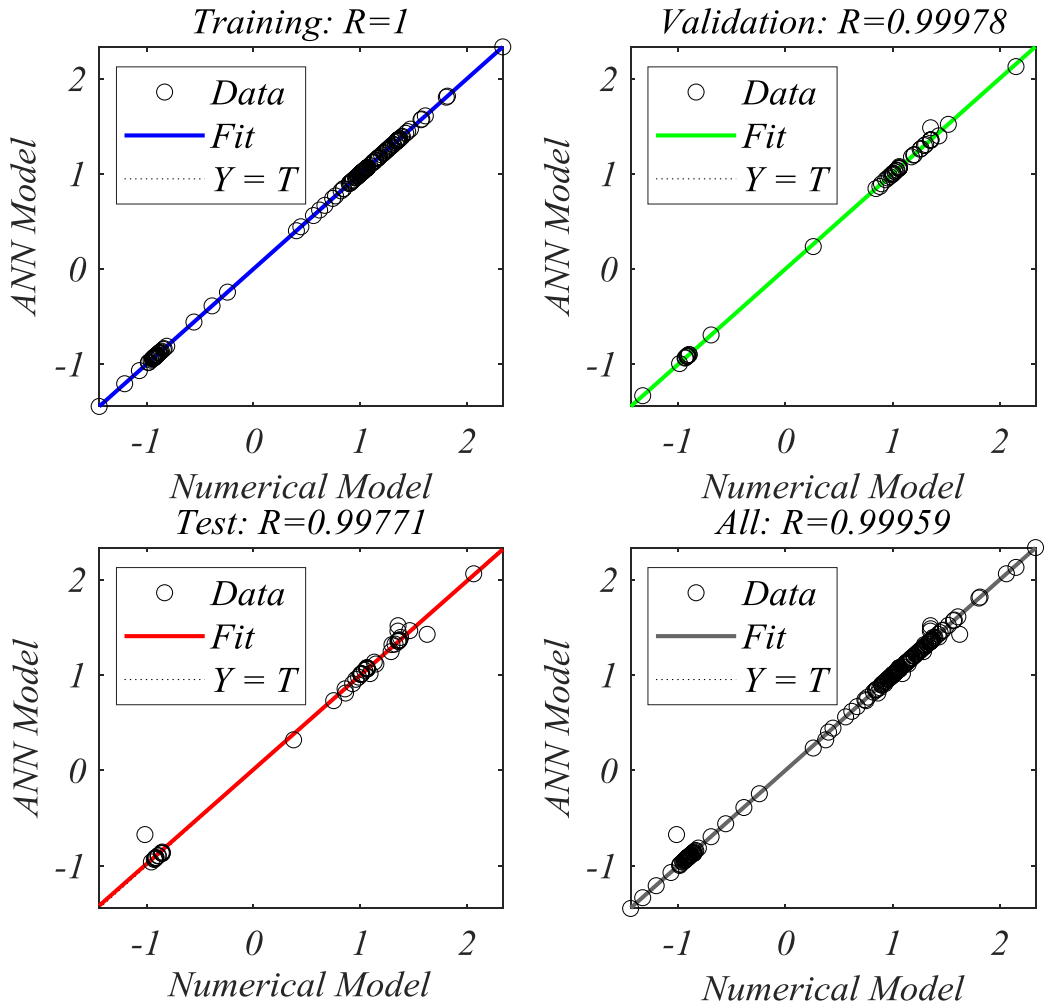

Figure 3 Statistical analysis with data from $\left(1/2C_f\,\mathrm{Re}_x^{1/2}\,X\right)$ $\left(Nu\,\mathrm{Re}_x^{-1/2}\,X^{-1}\right)$, $\left(Sh\,\mathrm{Re}_x^{-1/2}\right)$ and $\left(N_x\,\mathrm{Re}_x^{-1/2}\,X^{-1}\right)$.

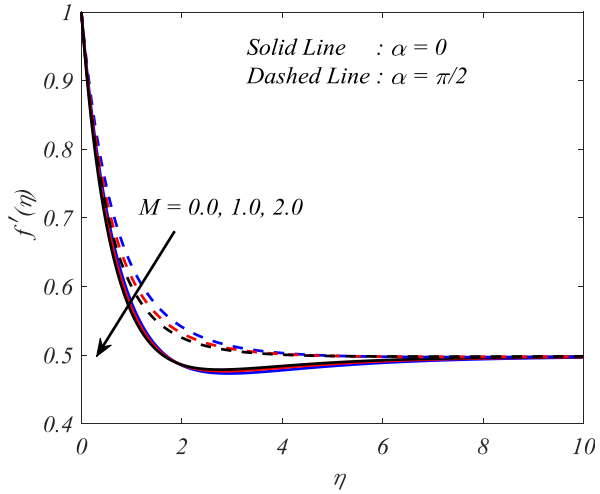

Figure 4 $f'(\eta)$ variation with M.

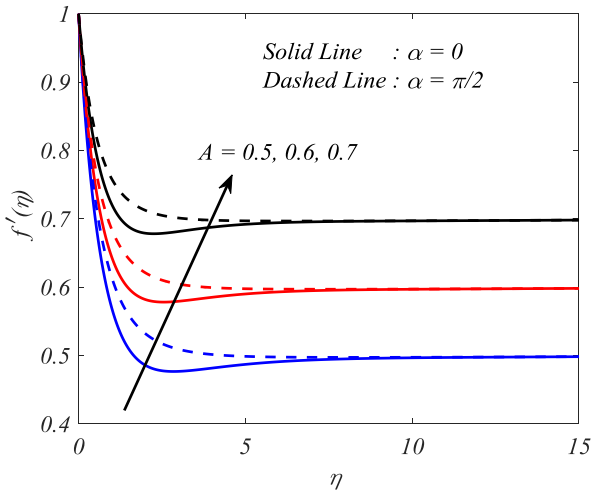

Figure 7 $f'(\eta)$ variation with A.

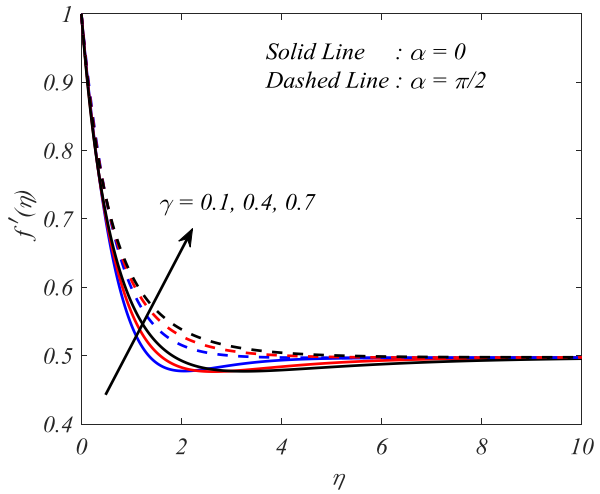

Figure 5 $f'(\eta)$ variation with γ.

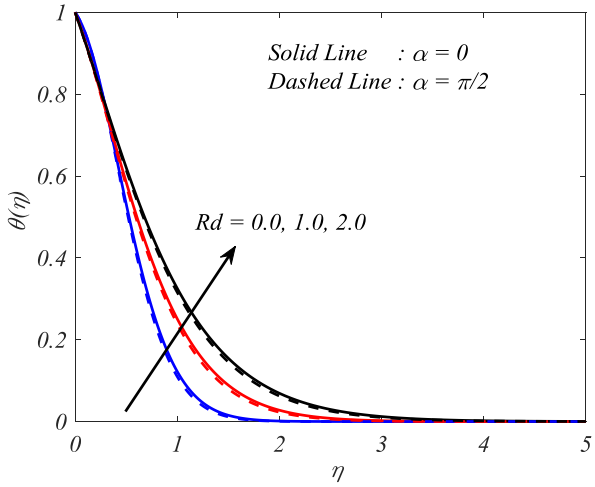

Figure 8 $\theta(\eta)$ variation with Rd.

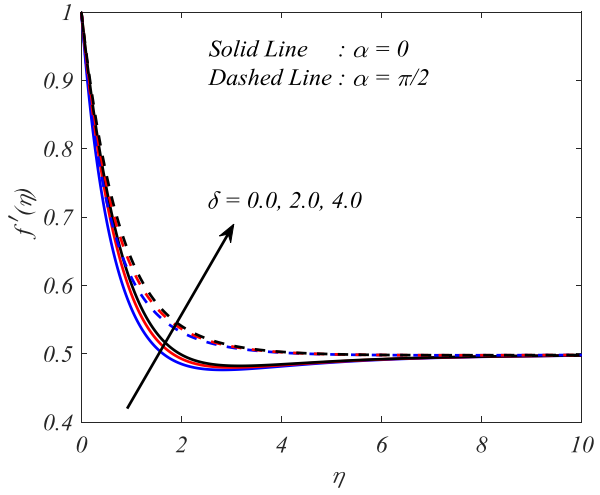

Figure 6 $f'(\eta)$ variation with δ.

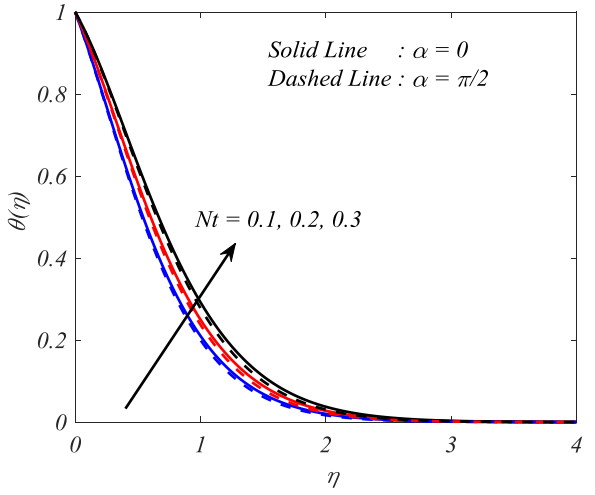

Figure 9 $\theta(\eta)$ variation with Nt.

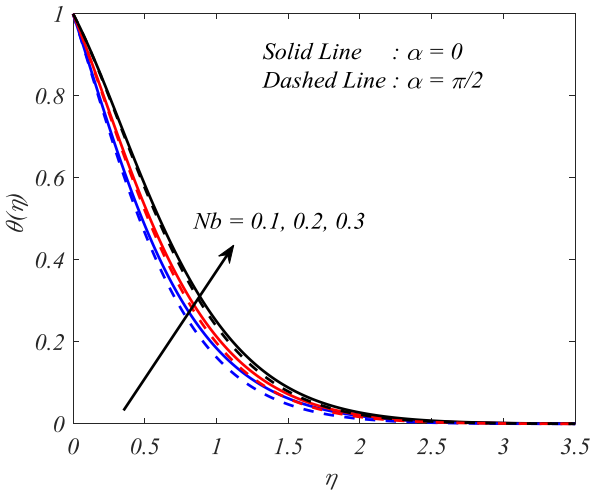

Figure 10 $\theta(\eta)$ variation with Nb.

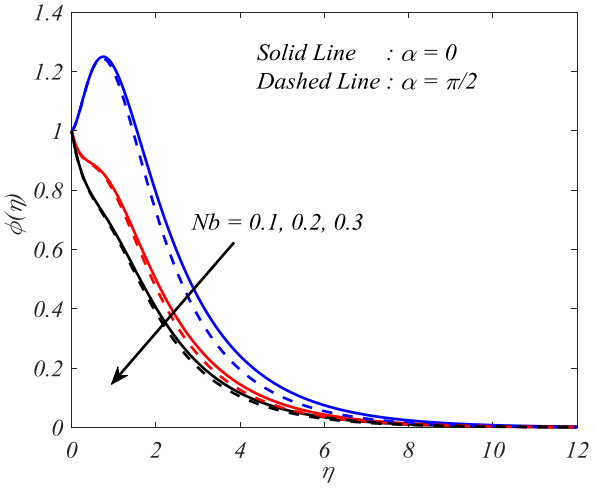

Figure 13 $\phi(\eta)$ variation with Nb.

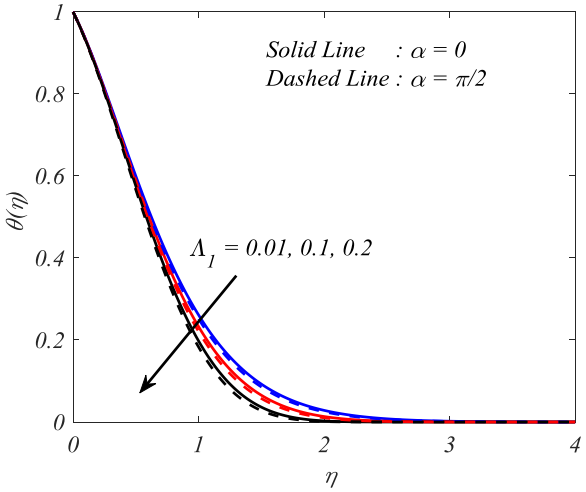

Figure 11 $\theta(\eta)$ variation with Λ_1.

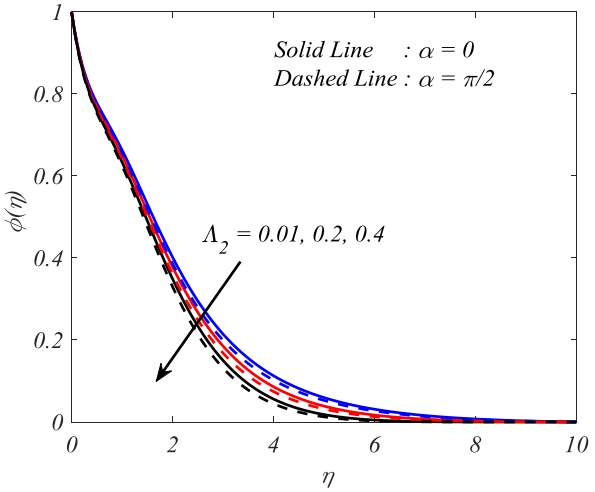

Figure 14 $\phi(\eta)$ variation with Λ_2.

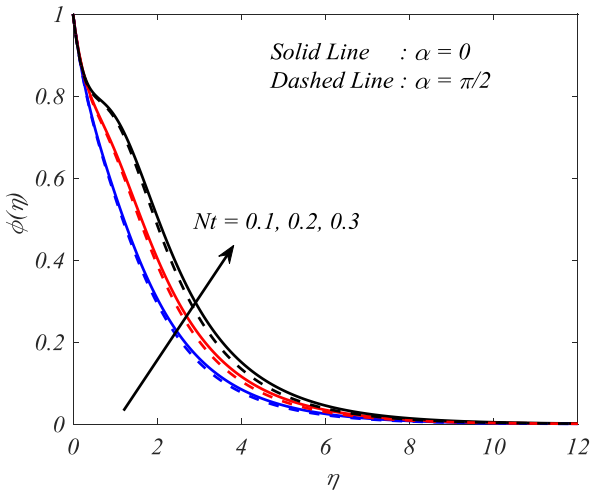

Figure 12 $\phi(\eta)$ variation with Nt.

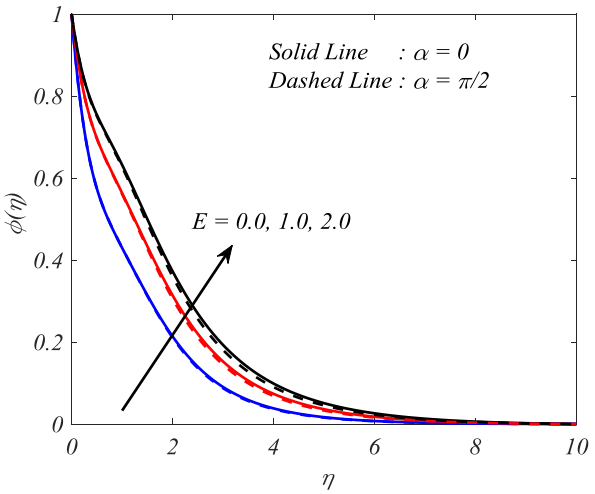

Figure 15 $\phi(\eta)$ variation with E.

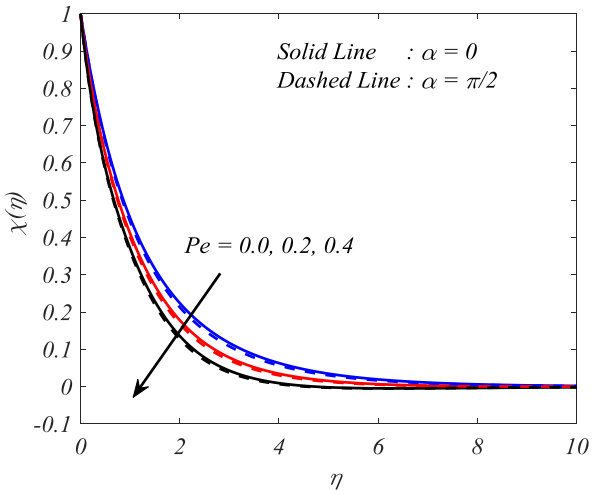

Figure 16 $\chi(\eta)$ variation with Pe.

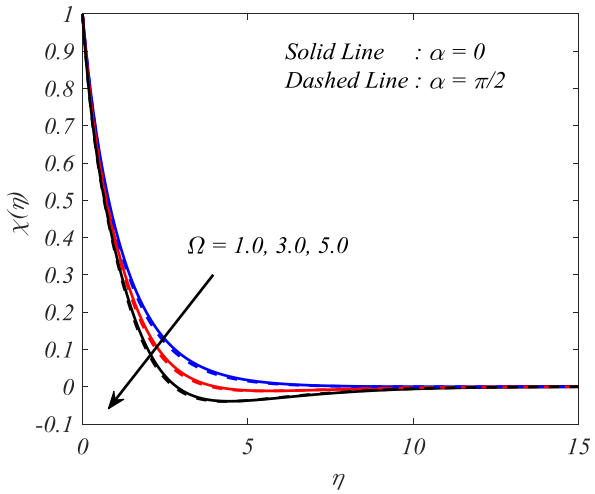

Figure 17 $\chi(\eta)$ variation with Ω.

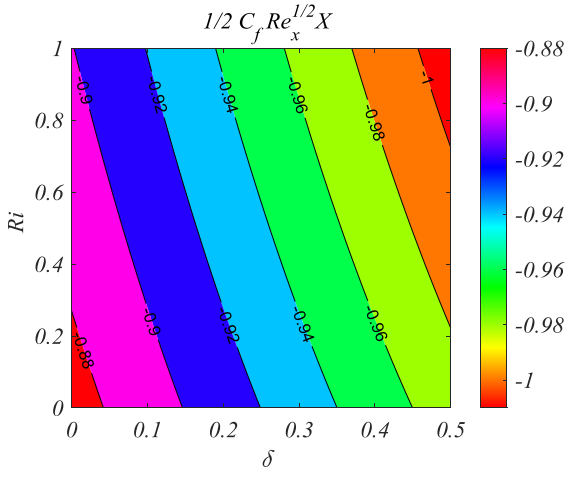

Figure 18 $1/2C_f\,\mathrm{Re}_x^{1/2}\,X$ variation with Ri and δ.

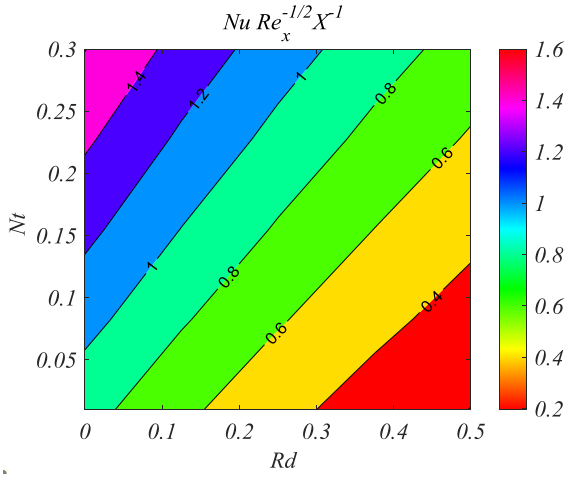

Figure 19 $Nu\,\mathrm{Re}_x^{-1/2}\,X^{-1}$ variation with Nt and Rd.

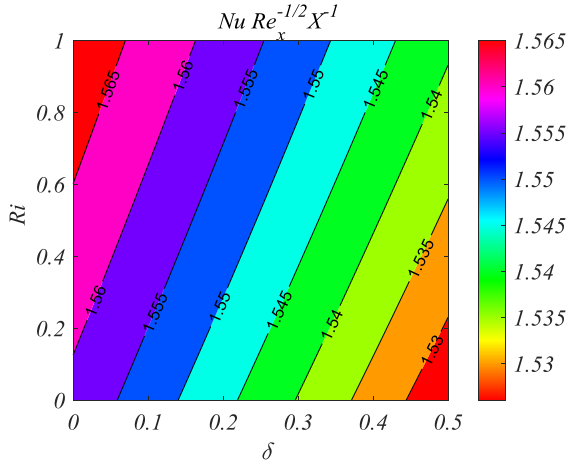

Figure 20 $Nu\,\mathrm{Re}_x^{-1/2}\,X^{-1}$ variation with Ri and δ.

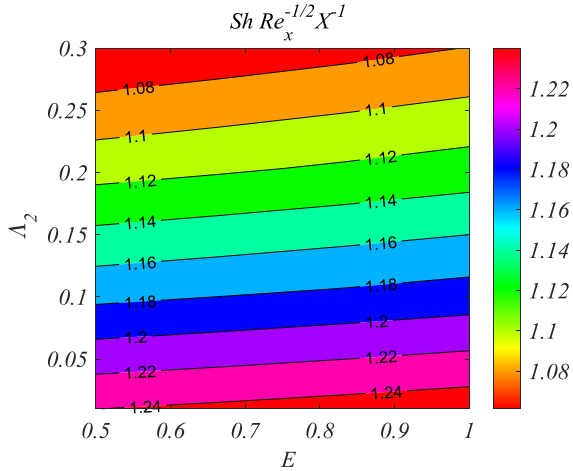

Figure 21 $Sh\,\mathrm{Re}_x^{-1/2}\,X^{-1}$ variation with Λ_2 and E.

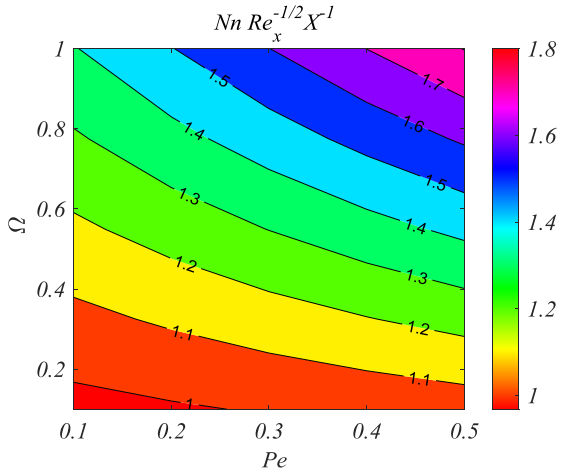

Figure 22 $Nn\,\mathrm{Re}_x^{-1/2}\,X^{-1}$ variation with Ω and Pe .

Table 1. Artificial neural network (ANN) and Numerical method values of $1/2C_f\,\mathrm{Re}_x^{1/2}\,X$.

γ	A	ε	δ	M	Ri	Nc	Nr	$1/2C_f\,\mathrm{Re}_x^{1/2}\,X$		
								NM	ANN	Error
0.2	0.5	1	0.2	0.5	0.5	0.5	0.5	-0.856	-0.86432	8.31E-03
0.4	0.5	1	0.2	0.5	0.5	0.5	0.5	-0.89846	-0.89927	8.14E-04
0.6	0.5	1	0.2	0.5	0.5	0.5	0.5	-0.93962	-0.93962	1.17E-08
0.8	0.5	1	0.2	0.5	0.5	0.5	0.5	-0.97977	-0.97977	9.29E-09
0.5	0.1	1	0.2	0.5	0.5	0.5	0.5	-1.4451	-1.4451	5.87E-09
0.5	0.2	1	0.2	0.5	0.5	0.5	0.5	-1.33245	-1.33223	2.20E-04
0.5	0.3	1	0.2	0.5	0.5	0.5	0.5	-1.2065	-1.2065	1.48E-07
0.5	0.4	1	0.2	0.5	0.5	0.5	0.5	-1.06836	-1.06836	1.62E-07
0.5	0.5	0.2	0.2	0.5	0.5	0.5	0.5	-0.38792	-0.38792	2.81E-08
0.5	0.5	0.4	0.2	0.5	0.5	0.5	0.5	-0.55774	-0.55774	1.56E-08
0.5	0.5	0.6	0.2	0.5	0.5	0.5	0.5	-0.69411	-0.69366	4.47E-04
0.5	0.5	0.8	0.2	0.5	0.5	0.5	0.5	-0.8125	-0.8125	6.46E-09
0.5	0.5	1	0.3	0.5	0.5	0.5	0.5	-0.92547	-0.92599	5.24E-04
0.5	0.5	1	0.4	0.5	0.5	0.5	0.5	-0.93149	-0.93149	4.18E-09
0.5	0.5	1	0.5	0.5	0.5	0.5	0.5	-0.93728	-0.93651	7.72E-04
0.5	0.5	1	0.6	0.5	0.5	0.5	0.5	-0.94287	-0.94287	7.72E-09
0.5	0.5	1	0.2	0	0.5	0.5	0.5	-0.83707	-0.83707	4.73E-06
0.5	0.5	1	0.2	0.15	0.5	0.5	0.5	-0.86246	-0.86245	1.23E-05
0.5	0.5	1	0.2	0.3	0.5	0.5	0.5	-0.88718	-0.88719	8.67E-06
0.5	0.5	1	0.2	0.45	0.5	0.5	0.5	-0.91128	-0.91129	4.64E-06
0.5	0.5	1	0.2	0.5	0.1	0.5	0.5	-0.89071	-0.8908	8.69E-05

0.5	0.5	1	0.2	0.5	0.2	0.5	0.5	-0.89779	-0.8978	1.44E-06
0.5	0.5	1	0.2	0.5	0.3	0.5	0.5	-0.9049	-0.9049	4.42E-06
0.5	0.5	1	0.2	0.5	0.4	0.5	0.5	-0.91203	-0.91203	4.50E-06
0.5	0.5	1	0.2	0.5	0.5	0.1	0.5	-0.85421	-0.85423	2.59E-05
0.5	0.5	1	0.2	0.5	0.5	0.2	0.5	-0.87035	-0.87035	1.10E-06
0.5	0.5	1	0.2	0.5	0.5	0.3	0.5	-0.88656	-0.88656	2.91E-06
0.5	0.5	1	0.2	0.5	0.5	0.4	0.5	-0.90284	-0.90284	2.38E-06
0.5	0.5	1	0.2	0.5	0.5	0.5	0.1	-0.84482	-0.84482	6.24E-09
0.5	0.5	1	0.2	0.5	0.5	0.5	0.2	-0.86329	-0.86338	9.02E-05
0.5	0.5	1	0.2	0.5	0.5	0.5	0.3	-0.88184	-0.88184	3.03E-09
0.5	0.5	1	0.2	0.5	0.5	0.5	0.4	-0.90047	-0.90036	1.10E-04

Table 2. Artificial neural network (ANN) and Numerical method values of $Nu\,\mathrm{Re}_x^{-1/2}\,X^{-1}$.

γ	A	ε	δ	Ri	Rd	Nb	Nt	Q	Λ_1	$Nu\,\mathrm{Re}_x^{-1/2}\,X^{-1}$		
										NM	ANN	Error
0.2	0.5	1	0.2	0.5	1	0.3	0.2	0.1	0.01	1.377561	1.393351	1.58E-02
0.4	0.5	1	0.2	0.5	1	0.3	0.2	0.1	0.01	1.357161	1.358349	1.19E-03
0.6	0.5	1	0.2	0.5	1	0.3	0.2	0.1	0.01	1.348286	1.348286	2.68E-08
0.8	0.5	1	0.2	0.5	1	0.3	0.2	0.1	0.01	1.347633	1.347633	1.28E-08
0.5	0.1	1	0.2	0.5	1	0.3	0.2	0.1	0.01	1.13887	1.13887	2.40E-08
0.5	0.2	1	0.2	0.5	1	0.3	0.2	0.1	0.01	1.202696	1.202292	4.04E-04
0.5	0.3	1	0.2	0.5	1	0.3	0.2	0.1	0.01	1.256444	1.256445	6.95E-08
0.5	0.4	1	0.2	0.5	1	0.3	0.2	0.1	0.01	1.305427	1.305427	7.28E-08
0.5	0.5	0.2	0.2	0.5	1	0.3	0.2	0.1	0.01	1.161937	1.161937	8.53E-08
0.5	0.5	0.4	0.2	0.5	1	0.3	0.2	0.1	0.01	1.248216	1.248216	5.18E-08
0.5	0.5	0.6	0.2	0.5	1	0.3	0.2	0.1	0.01	1.296608	1.296668	5.97E-05
0.5	0.5	0.8	0.2	0.5	1	0.3	0.2	0.1	0.01	1.328532	1.328532	5.61E-08
0.5	0.5	1	0.3	0.5	1	0.3	0.2	0.1	0.01	1.353769	1.35519	1.42E-03
0.5	0.5	1	0.4	0.5	1	0.3	0.2	0.1	0.01	1.355886	1.355886	2.17E-08
0.5	0.5	1	0.5	0.5	1	0.3	0.2	0.1	0.01	1.357886	1.355537	2.35E-03
0.5	0.5	1	0.6	0.5	1	0.3	0.2	0.1	0.01	1.359781	1.359781	2.10E-08
0.5	0.5	1	0.2	0.1	1	0.3	0.2	0.1	0.01	1.362925	1.362927	2.08E-06
0.5	0.5	1	0.2	0.2	1	0.3	0.2	0.1	0.01	1.360118	1.360118	3.48E-07
0.5	0.5	1	0.2	0.3	1	0.3	0.2	0.1	0.01	1.357282	1.357283	9.29E-07
0.5	0.5	1	0.2	0.4	1	0.3	0.2	0.1	0.01	1.354416	1.354414	1.06E-06
0.5	0.5	1	0.2	0.5	0.2	0.3	0.2	0.1	0.01	0.443591	0.443591	2.73E-07
0.5	0.5	1	0.2	0.5	0.4	0.3	0.2	0.1	0.01	0.668951	0.668952	1.32E-06
0.5	0.5	1	0.2	0.5	0.6	0.3	0.2	0.1	0.01	0.897832	0.89783	2.43E-06

0.5	0.5	1	0.2	0.5	0.8	0.3	0.2	0.1	0.01	1.126047	1.126049	1.88E-06
0.5	0.5	1	0.2	0.5	1	0.1	0.2	0.1	0.01	2.334367	2.334367	4.70E-09
0.5	0.5	1	0.2	0.5	1	0.15	0.2	0.1	0.01	2.062188	2.060346	1.84E-03
0.5	0.5	1	0.2	0.5	1	0.2	0.2	0.1	0.01	1.805833	1.805833	2.99E-08
0.5	0.5	1	0.2	0.5	1	0.25	0.2	0.1	0.01	1.56873	1.56873	1.22E-08
0.5	0.5	1	0.2	0.5	1	0.3	0.25	0.1	0.01	1.19948	1.19948	5.51E-09
0.5	0.5	1	0.2	0.5	1	0.3	0.3	0.1	0.01	1.060995	1.060995	1.55E-08
0.5	0.5	1	0.2	0.5	1	0.3	0.35	0.1	0.01	0.935057	0.937175	2.12E-03
0.5	0.5	1	0.2	0.5	1	0.3	0.4	0.1	0.01	0.820692	0.820692	8.11E-09
0.5	0.5	1	0.2	0.5	1	0.3	0.2	0.2	0.01	0.897126	0.897126	4.51E-09
0.5	0.5	1	0.2	0.5	1	0.3	0.2	0.3	0.01	0.375753	0.320942	5.48E-02
0.5	0.5	1	0.2	0.5	1	0.3	0.2	0.4	0.01	-0.24349	-0.24349	3.23E-08
0.5	0.5	1	0.2	0.5	1	0.3	0.2	0.5	0.01	-1.01657	-0.67101	3.46E-01
0.5	0.5	1	0.2	0.5	1	0.3	0.2	0.1	0.02	1.352533	1.352533	5.28E-08
0.5	0.5	1	0.2	0.5	1	0.3	0.2	0.1	0.03	1.353549	1.353549	3.15E-09
0.5	0.5	1	0.2	0.5	1	0.3	0.2	0.1	0.04	1.354569	1.353466	1.10E-03
0.5	0.5	1	0.2	0.5	1	0.3	0.2	0.1	0.05	1.355591	1.3511	4.49E-03

Table 3. Artificial neural network (ANN) and Numerical method values of $Sh\,\mathrm{Re}_x^{-1/2}\,X^{-1}$.

γ	ε	δ	Nr	Nb	Nt	Sc	Γ	θ_w	E	Λ_2	$Sh\,\mathrm{Re}_x^{-1/2}\,X^{-1}$		
											NM	ANN	Error
0.2	1	0.2	0.5	0.3	0.2	1	1	0.5	1	0.01	0.862574	0.811141	5.14E-02
0.4	1	0.2	0.5	0.3	0.2	1	1	0.5	1	0.01	0.997403	0.992454	4.95E-03
0.6	1	0.2	0.5	0.3	0.2	1	1	0.5	1	0.01	1.123547	1.123547	7.21E-09
0.8	1	0.2	0.5	0.3	0.2	1	1	0.5	1	0.01	1.242808	1.242807	1.06E-08
0.5	0.2	0.2	0.5	0.3	0.2	1	1	0.5	1	0.01	1.053035	1.053035	2.01E-08
0.5	0.4	0.2	0.5	0.3	0.2	1	1	0.5	1	0.01	1.053246	1.053246	3.28E-09
0.5	0.6	0.2	0.5	0.3	0.2	1	1	0.5	1	0.01	1.055709	1.055664	4.51E-05
0.5	0.8	0.2	0.5	0.3	0.2	1	1	0.5	1	0.01	1.058592	1.058592	2.76E-08
0.5	1	0.3	0.5	0.3	0.2	1	1	0.5	1	0.01	1.061503	1.061754	2.51E-04
0.5	1	0.4	0.5	0.3	0.2	1	1	0.5	1	0.01	1.061572	1.061572	4.51E-09
0.5	1	0.5	0.5	0.3	0.2	1	1	0.5	1	0.01	1.061643	1.061316	3.27E-04
0.5	1	0.6	0.5	0.3	0.2	1	1	0.5	1	0.01	1.061717	1.061717	8.82E-09
0.5	1	0.2	0.1	0.3	0.2	1	1	0.5	1	0.01	1.0654	1.0654	1.48E-08
0.5	1	0.2	0.2	0.3	0.2	1	1	0.5	1	0.01	1.064419	1.066345	1.93E-03
0.5	1	0.2	0.3	0.3	0.2	1	1	0.5	1	0.01	1.063431	1.063431	7.06E-09
0.5	1	0.2	0.4	0.3	0.2	1	1	0.5	1	0.01	1.062437	1.061037	1.40E-03
0.5	1	0.2	0.5	0.1	0.2	1	1	0.5	1	0.01	0.401997	0.401997	4.83E-08
0.5	1	0.2	0.5	0.15	0.2	1	1	0.5	1	0.01	0.750979	0.731291	1.97E-02

0.5	1	0.2	0.5	0.2	0.2	1	1	0.5	1	0.01	0.916107	0.916107	7.58E-08
0.5	1	0.2	0.5	0.25	0.2	1	1	0.5	1	0.01	1.007246	1.007246	7.21E-08
0.5	1	0.2	0.5	0.3	0.25	1	1	0.5	1	0.01	1.115031	1.115031	2.57E-08
0.5	1	0.2	0.5	0.3	0.3	1	1	0.5	1	0.01	1.181046	1.181046	4.20E-08
0.5	1	0.2	0.5	0.3	0.35	1	1	0.5	1	0.01	1.257195	1.25821	1.02E-03
0.5	1	0.2	0.5	0.3	0.4	1	1	0.5	1	0.01	1.341462	1.341462	1.48E-08
0.5	1	0.2	0.5	0.3	0.2	0.2	1	0.5	1	0.01	0.259452	0.235326	2.41E-02
0.5	1	0.2	0.5	0.3	0.2	0.4	1	0.5	1	0.01	0.561353	0.561353	7.06E-09
0.5	1	0.2	0.5	0.3	0.2	0.6	1	0.5	1	0.01	0.768081	0.768081	2.70E-09
0.5	1	0.2	0.5	0.3	0.2	0.8	1	0.5	1	0.01	0.928579	0.909389	1.92E-02
0.5	1	0.2	0.5	0.3	0.2	1	0.2	0.5	1	0.01	0.844885	0.845257	3.72E-04
0.5	1	0.2	0.5	0.3	0.2	1	0.4	0.5	1	0.01	0.907112	0.907112	5.82E-08
0.5	1	0.2	0.5	0.3	0.2	1	0.6	0.5	1	0.01	0.963255	0.963254	2.12E-07
0.5	1	0.2	0.5	0.3	0.2	1	0.8	0.5	1	0.01	1.014418	1.014419	2.52E-07
0.5	1	0.2	0.5	0.3	0.2	1	1	0.8	1	0.01	1.130753	1.134878	4.12E-03
0.5	1	0.2	0.5	0.3	0.2	1	1	1	1	0.01	1.176446	1.178391	1.95E-03
0.5	1	0.2	0.5	0.3	0.2	1	1	1.2	1	0.01	1.220318	1.220318	1.79E-09
0.5	1	0.2	0.5	0.3	0.2	1	1	1.4	1	0.01	1.262045	1.262045	3.36E-09
0.5	1	0.2	0.5	0.3	0.2	1	1	0.5	0.2	0.01	1.39428	1.39428	6.84E-09
0.5	1	0.2	0.5	0.3	0.2	1	1	0.5	0.4	0.01	1.286526	1.286526	2.35E-08
0.5	1	0.2	0.5	0.3	0.2	1	1	0.5	0.6	0.01	1.197227	1.196768	4.59E-04
0.5	1	0.2	0.5	0.3	0.2	1	1	0.5	0.8	0.01	1.123067	1.123067	4.42E-10
0.5	1	0.2	0.5	0.3	0.2	1	1	0.5	1	0.02	1.062036	1.062044	8.12E-06
0.5	1	0.2	0.5	0.3	0.2	1	1	0.5	1	0.04	1.063244	1.06324	3.65E-06
0.5	1	0.2	0.5	0.3	0.2	1	1	0.5	1	0.06	1.064464	1.064464	2.05E-07
0.5	1	0.2	0.5	0.3	0.2	1	1	0.5	1	0.08	1.065697	1.065697	5.19E-07

Table 4. Artificial neural network (ANN) and Numerical method values of $Nn\,\mathrm{Re}_x^{-1/2}\,X^{-1}$.

γ	A	ε	δ	M	Nc	Pe	Sb	Ω	$Nn\,\mathrm{Re}_x^{-1/2}\,X^{-1}$		
									NM	ANN	Error
0.2	0.5	1	0.2	0.5	0.5	0.1	1	0.5	0.857494	0.854728	2.77E-03
0.4	0.5	1	0.2	0.5	0.5	0.1	1	0.5	0.956104	0.955943	1.61E-04
0.6	0.5	1	0.2	0.5	0.5	0.1	1	0.5	1.051524	1.051524	1.10E-08
0.8	0.5	1	0.2	0.5	0.5	0.1	1	0.5	1.144169	1.144169	6.63E-09
0.5	0.1	1	0.2	0.5	0.5	0.1	1	0.5	0.845034	0.845034	2.34E-08
0.5	0.2	1	0.2	0.5	0.5	0.1	1	0.5	0.896244	0.895472	7.73E-04
0.5	0.3	1	0.2	0.5	0.5	0.1	1	0.5	0.936702	0.936702	8.28E-08
0.5	0.4	1	0.2	0.5	0.5	0.1	1	0.5	0.972002	0.972002	9.83E-08

0.5	0.5	0.2	0.2	0.5	0.5	0.1	1	0.5	0.955319	0.955319	3.99E-09
0.5	0.5	0.4	0.2	0.5	0.5	0.1	1	0.5	0.974017	0.974017	1.09E-08
0.5	0.5	0.6	0.2	0.5	0.5	0.1	1	0.5	0.9868	0.986643	1.57E-04
0.5	0.5	0.8	0.2	0.5	0.5	0.1	1	0.5	0.99647	0.99647	3.26E-09
0.5	0.5	1	0.3	0.5	0.5	0.1	1	0.5	1.004741	1.004672	6.86E-05
0.5	0.5	1	0.4	0.5	0.5	0.1	1	0.5	1.005268	1.005268	4.79E-09
0.5	0.5	1	0.5	0.5	0.5	0.1	1	0.5	1.005772	1.006012	2.40E-04
0.5	0.5	1	0.6	0.5	0.5	0.1	1	0.5	1.006255	1.006255	6.04E-09
0.5	0.5	1	0.2	0	0.5	0.1	1	0.5	1.009025	1.009021	3.57E-06
0.5	0.5	1	0.2	0.15	0.5	0.1	1	0.5	1.007484	1.007493	9.13E-06
0.5	0.5	1	0.2	0.3	0.5	0.1	1	0.5	1.006022	1.006014	7.80E-06
0.5	0.5	1	0.2	0.45	0.5	0.1	1	0.5	1.004634	1.004637	3.10E-06
0.5	0.5	1	0.2	0.5	0.1	0.1	1	0.5	1.010341	1.010445	1.04E-04
0.5	0.5	1	0.2	0.5	0.2	0.1	1	0.5	1.008822	1.008826	3.68E-06
0.5	0.5	1	0.2	0.5	0.3	0.1	1	0.5	1.00729	1.007279	1.10E-05
0.5	0.5	1	0.2	0.5	0.4	0.1	1	0.5	1.005746	1.005756	1.09E-05
0.5	0.5	1	0.2	0.5	0.5	0.2	1	0.5	1.146177	1.114978	3.12E-02
0.5	0.5	1	0.2	0.5	0.5	0.3	1	0.5	1.288816	1.24507	4.37E-02
0.5	0.5	1	0.2	0.5	0.5	0.4	1	0.5	1.432077	1.398904	3.32E-02
0.5	0.5	1	0.2	0.5	0.5	0.5	1	0.5	1.575936	1.575936	2.60E-10
0.5	0.5	1	0.2	0.5	0.5	0.1	0.2	0.5	0.619313	0.619313	1.34E-07
0.5	0.5	1	0.2	0.5	0.5	0.1	0.4	0.5	0.741594	0.741593	6.36E-07
0.5	0.5	1	0.2	0.5	0.5	0.1	0.6	0.5	0.841092	0.841093	1.30E-06
0.5	0.5	1	0.2	0.5	0.5	0.1	0.8	0.5	0.927119	0.927118	1.12E-06
0.5	0.5	1	0.2	0.5	0.5	0.1	1	0.6	1.013155	1.013144	1.02E-05
0.5	0.5	1	0.2	0.5	0.5	0.1	1	0.7	1.022122	1.022132	9.37E-06
0.5	0.5	1	0.2	0.5	0.5	0.1	1	0.8	1.03109	1.031087	2.87E-06
0.5	0.5	1	0.2	0.5	0.5	0.1	1	0.9	1.040058	1.039927	1.30E-04

Table 5. The $-f''(0)$ values are compared across various M values with those presented by Vajravelu et al. [45]).

		M = 0.0	M = 0.5	M = 1.0	M = 1.5	M = 2.0
Vajravelu et al. [45]	Keller-box method	1.000001	1.224745	1.414214	1.581139	1.732051
	Analytical solution	1	1.224745	1.414214	1.581139	1.732051
Present values		1	1.224745	1.414214	1.581139	1.732051

Appendix A: List of Figures

Figure 1 Geometry of the problem.

Figure 2 An ANN model with several layers is shown schematically.

Figure 3 Statistical analysis with data from $\left(1/2C_f \,\mathrm{Re}_x^{1/2}\, X\right)$, $\left(Nu\,\mathrm{Re}_x^{-1/2}\, X^{-1}\right)$, $\left(Sh\,\mathrm{Re}_x^{-1/2}\right)$ and $\left(N_x\,\mathrm{Re}_x^{-1/2}\, X^{-1}\right)$.

Figure 4 $f'(\eta)$ variation with M.

Figure 5 $f'(\eta)$ variation with γ.

Figure 6 $f'(\eta)$ variation with δ.

Figure 7 $f'(\eta)$ variation with A.

Figure 8 $\theta(\eta)$ variation with Rd.

Figure 9 $\theta(\eta)$ variation with Nt.

Figure 10 $\theta(\eta)$ variation with Nb.

Figure 11 $\theta(\eta)$ variation with Λ_1.

Figure 12 $\phi(\eta)$ variation with Nt.

Figure 13 $\phi(\eta)$ variation with Nb.

Figure 14 $\phi(\eta)$ variation with Λ_2.

Figure 15 $\phi(\eta)$ variation with E.

Figure 16 $\chi(\eta)$ variation with Pe.

Figure 17 $\chi(\eta)$ variation with Ω.

Figure 18 $1/2C_f \,\mathrm{Re}_x^{1/2}\, X$ variation with Ri and δ.

Figure 19 $Nu\,\mathrm{Re}_x^{-1/2}\, X^{-1}$ variation with Nt and Rd.

Figure 20 $Nu\,\mathrm{Re}_x^{-1/2}\, X^{-1}$ variation with Ri and δ.

Figure 21 $Sh\,\mathrm{Re}_x^{-1/2}\,X^{-1}$ variation with Λ_2 and E.

Figure 22 $Nn\,\mathrm{Re}_x^{-1/2}\,X^{-1}$ variation with Ω and Pe.

Appendix B: Table of Contents

Table 1. Artificial neural network (ANN) and Numerical method values of $1/2C_f\,\mathrm{Re}_x^{1/2}\,X$.

Table 2. Artificial neural network (ANN) and Numerical method values of $Nu\,\mathrm{Re}_x^{-1/2}\,X^{-1}$.

Table 3. Artificial neural network (ANN) and Numerical method values of $Sh\,\mathrm{Re}_x^{-1/2}\,X^{-1}$.

Table 4. Artificial neural network (ANN) and Numerical method values of $Nn\,\mathrm{Re}_x^{-1/2}\,X^{-1}$.

Table 5. The $-f''(0)$ values are compared across various *M* values with those presented by Vajravelu et al. [45]).